7

Frequency-Domain Numerical Modelling of Visco-Acoustic Waves with Finite-Difference and Finite-Element Discontinuous Galerkin Methods

Romain Brossier[1,2], Vincent Etienne[1], Stéphane Operto[1] and Jean Virieux[2]
[1]*Geoazur - CNRS - UNSA - IRD – OCA*
[2]*LGIT - University Joseph Fourier*
France

1. Introduction

Seismic exploration is one of the main geophysical methods to extract quantitative inferences about the Earth's interior at different scales from the recording of seismic waves near the surface. Main applications are civil engineering for cavity detection and landslide characterization, site effect modelling for seismic hazard, CO_2 sequestration and nuclear-waste storage, oil and gas exploration, and fundamental understanding of geodynamical processes. Acoustic or elastic waves are emitted either by controlled sources or natural sources (i.e., earthquakes). Interactions of seismic waves with the heterogeneities of the subsurface provide indirect measurements of the physical properties of the subsurface which govern the propagation of elastic waves (compressional and shear wave speeds, density, attenuation, anisotropy). Quantitative inference of the physical properties of the subsurface from the recordings of seismic waves at receiver positions is the so-called seismic inverse problem that can be recast in the framework of local numerical optimization. The most complete seismic inversion method, the so-called full waveform inversion (Virieux & Operto (2009) for a review), aims to exploit the full information content of seismic data by minimization of the misfit between the full seismic wavefield and the modelled one. The theoretical resolution of full waveform inversion is half the propagated wavelength. In full waveform inversion, the full seismic wavefield is generally modelled with volumetric methods that rely on the discretization of the wave equation (finite difference, finite element, finite volume methods).

In the regime of small deformations associated with seismic wave propagation, the subsurface can be represented by a linear elastic solid parameterized by twenty-one elastic constants and the density in the framework of the constitutive Hooke's law. If the subsurface is assumed isotropic, the elastic constants reduce to two independent parameters, the Lamé parameters, which depend on the compressional (P) and the shear (S) wave speeds. In marine environment, the P wave speed has most of the time a dominant footprint in the seismic wavefield, in particular, on the hydrophone component which records the pressure wavefield. The dominant footprint of the P wave speed on the seismic

Source: Acoustic Waves, Book edited by: Don W. Dissanayake,
ISBN 978-953-307-111-4, pp. 466, September 2010, Sciyo, Croatia, downloaded from SCIYO.COM

wavefield has prompted many authors to develop and apply seismic modelling and inversion under the acoustic approximation, either in the time domain or in the frequency domain.

This study focuses on frequency-domain modelling of acoustic waves as a tool to perform seismic imaging in the acoustic approximation. In the frequency-domain, wave modelling reduces to the resolution of a complex-valued large and sparse system of linear equations for each frequency, the solution of which is the monochromatic wavefield and the right-hand side (r.h.s) is the source. Two key issues in frequency-domain wave modelling concern the linear algebra technique used to solve the linear system and the numerical method used for the discretization of the wave equation. The linear system can be solved with Gauss elimination techniques based on sparse direct solver (e.g., Duff et al.; 1986), Krylov-subspace iterative methods (e.g., Saad; 2003) or hybrid direct/iterative method and domain decomposition techniques (e.g., Smith et al.; 1996). In the framework of seismic imaging applications which involve a large number of seismic sources (i.e., r.h.s), one motivation behind the frequency-domain formulation of acoustic wave modelling has been to develop efficient approaches for multi-r.h.s modelling based on sparse direct solvers (Marfurt; 1984). A sparse direct solver performs first a LU decomposition of the matrix which is independent of the source followed by forward and backward substitutions for each source to get the solution (Duff et al.; 1986). This strategy has been shown to be efficient for 2D applications of acoustic full waveform inversion on realistic synthetic and real data case studies (Virieux & Operto; 2009). Two drawbacks of the direct-solver approach are the memory requirement of the LU decomposition resulting from the fill-in of the matrix during the LU decomposition (namely, the additional non zero coefficients introduced during the elimination process) and the limited scalability of the LU decomposition on large-scale distributed-memory platforms. It has been shown however that large-scale 2D acoustic problems involving several millions of unknowns can be efficiently tackled thanks to recent development of high-performance parallel solvers (e.g., MUMPS team; 2009), while 3D acoustic case studies remain limited to computational domains involving few millions of unknowns (Operto et al.; 2007). An alternative approach to solve the time-harmonic wave equation is based on Krylov-subspace iterative solvers (Riyanti et al.; 2006; Plessix; 2007; Riyanti et al.; 2007). Iterative solvers are significantly less memory demanding than direct solvers but the computational time linearly increases with the number of r.h.s. Moreover, the impedance matrix, which results from the discretization of the wave equation, is indefinite (the real eigenvalues change sign), and therefore ill-conditioned. Designing efficient pre-conditioner for the Helmholtz equation is currently an active field of research (Erlangga & Nabben; 2008). Efficient preconditioners based on one cycle of multigrid applied to the damped wave equation have been developed and leads to a linear increase of the number of iterations with frequency when the grid interval is adapted to the frequency (Erlangga et al.; 2006). This makes the time complexity of the iterative approaches to be $\mathcal{O}(N^4)$, where N denotes the dimension of the 3D N^3 cubic grid. Intermediate approaches between the direct and iterative approaches are based on domain decomposition methods and hybrid direct/iterative solvers. In the hybrid approach, the iterative solver is used to solve a reduced system for interface unknowns shared by adjacent subdomains while the sparse direct solver is used to factorize local impedance matrices assembled on each subdomains during a preprocessing step (Haidar; 2008; Sourbier et al.; 2008). A short review of the time and memory complexities of the direct, iterative and hybrid approaches is provided in Virieux et al. (2009).

The second issue concerns the numerical scheme used to discretize the wave equation. Most of the methods that have been developed for seismic acoustic wave modelling in the frequency domain rely on the finite difference (FD) method. This can be justified by the fact that, in many geological environments such as offshore sedimentary basins, the subsurface of the earth can be viewed as a weakly-contrasted medium at the scale of the seismic wavelengths, for which FD methods on uniform grid provide the best compromise between accuracy and computational efficiency. In the FD time-domain method, high-order accurate stencils are generally designed to achieve the best trade-off between accuracy and computational efficiency (Dablain; 1986). However, direct-solver approaches in frequency-domain modelling prevent the use of such high-order accurate stencils because their large spatial support will lead to a prohibitive fill-in of the matrix during the LU decomposition (Stekl & Pratt; 1998; Hustedt et al.; 2004). Another discretization strategy, referred to as the mixed-grid approach, has been therefore developed to perform frequency-domain modelling with direct solver: it consists of the linear combination of second-order accurate stencils built on different rotated coordinate systems combined with an anti-lumped mass strategy, where the mass term is spatially distributed over the different nodes of the stencil (Jo et al.; 1996). The combination of these two tricks allows one to design both compact and accurate stencils in terms of numerical anisotropy and dispersion.

Sharp boundaries of arbitrary geometry such as the air-solid interface at the free surface are often discretized along staircase boundaries of the FD grid, although embedded boundary representation has been proposed (Lombard & Piraux; 2004; Lombard et al.; 2008; Mattsson et al.; 2009), and require dense grid meshing for accurate representation of the medium. The lack of flexibility to adapt the grid interval to local wavelengths, although some attempts have been performed in this direction (e.g., Pitarka; 1999; Taflove & Hagness; 2000), is another drawback of FD methods. These two limitations have prompted some authors to develop finite-element methods in the time domain for seismic wave modelling on unstructured meshes. The most popular one is the high-order spectral element method (Seriani & Priolo; 1994; Priolo et al.; 1994; Faccioli et al.; 1997) that has been popularized in the field of global scale seismology by Komatitsch and Vilotte (1998); Chaljub et al. (2007). A key feature of the spectral element method is the combined use of Lagrange interpolants and Gauss-Lobatto-Legendre quadrature that makes the mass matrix diagonal and, therefore, the numerical scheme explicit in time-marching algorithms, and allows for spectral convergence with high approximation orders (Komatitsch & Vilotte; 1998). The selected quadrature formulation leads to quadrangle (2D) and hexahedral (3D) meshes, which strongly limit the geometrical flexibility of the discretization. Alternatively, discontinuous form of the finite-element method, the so-called discontinuous Galerkin (DG) method (Hesthaven & Warburton; 2008), popularized in the field of seismology by Kaser, Dumbser and co-workers (e.g., Dumbser & Käser; 2006) has been developed. In the DG method, the numerical scheme is strictly kept local by duplicating variables located at nodes shared by neighboring cells. Consistency between the multiply defined variables is ensured by consistent estimation of numerical fluxes at the interface between two elements. Numerical fluxes at the interface are introduced in the weak form of the wave equation by means of integration by part followed by application of the Gauss's theorem. Key advantages of the DG method compared to the spectral element method is its capacity of considering triangular (2D) and tetrahedral (3D) non-conform meshes. Moreover, the uncoupling of the elements provides a higher level of flexibility to locally adapt the size of

the elements (*h* adaptivity) and the interpolation orders within each element (*p* adaptivity) because neighboring cells exchange information across interfaces only. Moreover, the DG method provides a suitable framework to implement any kind of physical boundary conditions involving possible discontinuity at the interface between elements. One example of application which takes fully advantage of the discontinuous nature of the DG method is the modelling of the rupture dynamics (BenJemaa et al.; 2007, 2009; de la Puente et al.; 2009).
The dramatic increase of the total number of degrees of freedom compared to standard finite-element methods, that results from the uncoupling of the elements, might prevent an efficient use of DG methods. This is especially penalizing for frequency-domain methods based on sparse direct solver where the computational cost scales with the size of the matrix N in $\mathcal{O}(N^6)$ for 3D problems. The increase of the size of the matrix should however be balanced by the fact the DG schemes are more local and sparser than FEM ones (Hesthaven & Warburton; 2008), which makes smaller the numerical bandwidth of the matrix to be factorized.
When a zero interpolation order is used in cells (piecewise constant solution), the DG method reduces to the finite volume method (LeVeque; 2002). The DG method based on high-interpolation orders has been mainly developed in the time domain for the elastodynamic equations (e.g., Dumbser & Käser; 2006). Implementation of the DG method in the frequency domain has been presented by Dolean et al. (2007, 2008) for the time-harmonic Maxwell equations and a domain decomposition method has been used to solve the linear system resulting from the discretization of the Maxwell equations. A parsimonious finite volume method on equilateral triangular mesh has been presented by Brossier et al. (2008) to solve the 2D P-SV elastodynamic equations in the frequency domain. The finite-volume approach of Brossier et al. (2008) has been extended to low-order DG method on unstructured triangular meshes in Brossier (2009).
We propose a review of these two quite different numerical methods, the mixed-grid FD method with simple regular-grid meshing and the DG method with dense unstructured meshing, when solving frequency-domain visco-acoustic wave propagation with sparse direct solver in different fields of application. After a short review of the time-harmonic visco-acoustic wave equation, we first review the mixed-grid FD method for 3D modelling. We first discuss the accuracy of the scheme which strongly relies on the optimization procedure designed to minimize the numerical dispersion and anisotropy. Some key features of the FD method such as the absorbing and free-surface boundary conditions and the source excitation on coarse FD grids are reviewed. Then, we present updated numerical experiments performed with the last release of the massively-parallel sparse direct solver MUMPS (Amestoy et al.; 2006). We first assess heuristically the memory complexity and the scalability of the LU factorization. Second, we present simulations in two realistic synthetic models representative of oil exploration targets. We assess the accuracy of the solutions and the computational efficiency of the mixed-grid FD frequency-domain method against that of a conventional FD time-domain method. In the second part of the study, we review the DG frequency-domain method applied to the first-order acoustic wave equation for pressure and particle velocities. After a review of the spatial discretization, we discuss the impact of the order of the interpolating Lagrange polynomials on the computational cost of the frequency-domain DG method and we present 2D numerical experiments on unstructured triangular meshes to highlight the fields of application where the DG method should outperform the FD method.

Although the numerical methods presented in this study were originally developed for seismic applications, they can provide a useful framework for other fields of application such as computational ocean acoustics (Jensen et al.; 1994) and electrodynamics (Taflove & Hagness; 2000).

2. Frequency-domain acoustic wave equation

Following standard Fourier transformation convention, the 3D acoustic first-order velocity-pressure system can be written in the frequency domain as

$$\begin{aligned} -i\omega p(x,y,z,\omega) &= \kappa(x,y,z)\left(\frac{\partial v_x(x,y,z,\omega)}{\partial x}+\frac{\partial v_y(x,y,z,\omega)}{\partial y}+\frac{\partial v_z(x,y,z,\omega)}{\partial z}\right) \\ -i\omega v_x(x,y,z,\omega) &= b(x,y,z)\cdot\frac{\partial p(x,y,z,\omega)}{\partial x}+f_x(x,y,z,\omega) \\ -i\omega v_y(x,y,z,\omega) &= b(x,y,z)\cdot\frac{\partial p(x,y,z,\omega)}{\partial y}+f_y(x,y,z,\omega) \\ -i\omega v_z(x,y,z,\omega) &= b(x,y,z)\cdot\frac{\partial p(x,y,z,\omega)}{\partial z}+f_z(x,y,z,\omega), \end{aligned} \tag{1}$$

where ω is the angular frequency, $\kappa(x, y, z)$ is the bulk modulus, $b(x, y, z)$ is the buoyancy, $p(x, y, z, \omega)$ is the pressure, $v_x(x, y, z, \omega)$, $v_y(x, y, z, \omega)$, $v_z(x, y, z, \omega)$ are the components of the particle velocity vector. $f_x(x, y, z, \omega)$, $f_y(x, y, z, \omega)$, $f_z(x, y, z, \omega)$ are the components of the external forces. The first block row of equation 1 is the time derivative of the Hooke's law, while the three last block rows are the equation of motion in the frequency domain.
The first-order system can be recast as a second-order equation in pressure after elimination of the particle velocities in equation 1, that leads to a generalization of the Helmholtz equation:

$$\frac{\omega^2}{\kappa(\mathbf{x})}p(\mathbf{x},\omega)+\frac{\partial}{\partial x}b(\mathbf{x})\frac{\partial p(\mathbf{x},\omega)}{\partial x}+\frac{\partial}{\partial y}b(\mathbf{x})\frac{\partial p(\mathbf{x},\omega)}{\partial y}+\frac{\partial}{\partial z}b(\mathbf{x})\frac{\partial p(\mathbf{x},\omega)}{\partial z}=s(\mathbf{x},\omega), \tag{2}$$

where $\mathbf{x} = (x,y, z)$ and $s(\mathbf{x},\omega) = \nabla \cdot \mathbf{f}$ denotes the pressure source. In exploration seismology, the source is generally a local point source corresponding to an explosion or a vertical force.
Attenuation effects of arbitrary complexity can be easily implemented in equation 2 using complex-valued wave speeds in the expression of the bulk modulus, thanks to the correspondence theorem transforming time convolution into products in the frequency domain. For example, according to the Kolsky-Futterman model (Kolsky; 1956; Futterman; 1962), the complex wave speed $\overline{c}$ is given by:

$$\overline{c}=c\left[\left(1+\frac{1}{\pi Q}\left|\log(\omega/\omega_r)\right|\right)+i\frac{sgn(\omega)}{2Q}\right]^{-1}, \tag{3}$$

where the P wave speed is denoted by c, the attenuation factor by Q and a reference frequency by ω_r.
Since the relationship between the wavefields and the source terms is linear in the first-order and second-order wave equations, equations 1 and 2 can be recast in matrix form:

$$\left[\mathbf{M}+\mathbf{S}\right]\mathbf{u}=\mathbf{A}\mathbf{u}=\mathbf{b}, \tag{4}$$

where $\mathbf{M}$ is the mass matrix, $\mathbf{S}$ is the complex stiffness/damping matrix. The sparse impedance matrix $\mathbf{A}$ has complex-valued coefficients which depend on medium properties and angular frequency. The wavefield (either the scalar pressure wavefield or the pressure-velocity wavefields) is denoted by the vector $\mathbf{u}$ and the source by $\mathbf{b}$ (Marfurt; 1984). The dimension of the square matrix $\mathbf{A}$ is the number of nodes in the computational domain multiplied by the number of wavefield components. The matrix $\mathbf{A}$ has a symmetric pattern for the FD method and the DG method discussed in this study but is generally not symmetric because of absorbing boundary conditions along the edges of the computational domain. In this study, we shall solve equation 4 by Gaussian elimination using sparse direct solver. A direct solver performs first a LU decomposition of $\mathbf{A}$ followed by forward and backward substitutions for the solutions (Duff et al.; 1986).

$$\mathbf{A}\mathbf{u}=\left(\mathbf{L}\mathbf{U}\right)\mathbf{u}=\mathbf{b} \tag{5}$$

$$\mathbf{L}\mathbf{y}=\mathbf{b}; \quad \mathbf{U}\mathbf{u}=\mathbf{y} \tag{6}$$

Exploration seismology requires to perform seismic modelling for a large number of sources, typically, up to few thousands for 3D acquisition. Therefore, our motivation behind the use of direct solver is the efficient computation of the solutions of the equation 4 for multiple sources. The LU decomposition of $\mathbf{A}$ is a time and memory demanding task but is independent of the source, and, therefore is performed only once, while the substitution phase provides the solution for multiple sources efficiently. One bottleneck of the direct-solver approach is the memory requirement of the LU decomposition resulting from the fill-in, namely, the creation of additional non-zero coefficients during the elimination process. This fill-in can be minimized by designing compact numerical stencils that allow for the minimization of the numerical bandwidth of the impedance matrix. In the following, we shall review a FD method and a finite-element DG method that allow us to fullfill this requirement.

3. Mixed-grid finite-difference method

3.1 Discretization of the differential operators

In FD methods, high-order accurate stencils are generally designed to achieve the best tradeoff between accuracy and computational efficiency (Dablain; 1986). However, direct-solver methods prevent the use of high-order accurate stencils because their large spatial support will lead to a prohibitive fill-in of the matrix during the LU decomposition (Hustedt et al.; 2004). Alternatively, the mixed-grid method was proposed by Jo et al. (1996) to design both accurate and compact FD stencils. The governing idea is to discretize the differential operators of the stiffness matrix with different second-order accurate stencils and to linearly combine the resulting stiffness matrices with appropriate weighting coefficients. The different stencils are built by discretizing the differential operators along different rotated coordinate systems ($\overline{x}$, $\overline{y}$, $\overline{z}$) such that their axes span as many directions as possible in the FD cell to mitigate numerical anisotropy. In practice, this means that the partial derivatives with respect to x, y and z in equations 1 or 2 are replaced by a linear combination of partial derivatives with respect to $\overline{x}$, $\overline{y}$ and $\overline{z}$ using the chain rule followed by the

discretization of the differential operators along the axis $\bar{x}$, $\bar{y}$ and $\bar{z}$. In 2D, the coordinate systems are the classic Cartesian one and the 45°-rotated one (Saenger et al.; 2000) which lead to the 9-point stencil (Jo et al.; 1996). In 3D, three coordinate systems have been identified (Operto et al.; 2007) (Figure 1): [1] the Cartesian one which leads to the 7-point stencil, [2] three coordinate systems obtained by rotating the Cartesian system around each Cartesian axis x, y, and z. Averaging of the three elementary stencils leads to a 19-point stencil. [3] four coordinate systems defined by the four main diagonals of the cubic cell. Averaging of the four elementary stencils leads to the 27-point stencil. The stiffness matrix associated with the 7-point stencil, the 19-point stencil and the 27-point stencil will be denoted by $\mathbf{S}_1$, $\mathbf{S}_2$, $\mathbf{S}_3$, respectively.
The mixed-grid stiffness matrix $\mathbf{S}_{mg}$ is a linear combination of the stiffness matrices just-mentioned:

$$\mathbf{S}_{mg} = w_1\mathbf{S}_1 + \frac{w_2}{3}\mathbf{S}_2 + \frac{w_3}{4}\mathbf{S}_3, \tag{7}$$

where we have introduced the weighting coefficients w_1, w_2 and w_3 which satisfy:

$$w_1 + w_2 + w_3 = 1 \tag{8}$$

In the original mixed-grid approach (Jo et al.; 1996), the discretization on the different coordinate systems was directly applied to the second-order wave equation, equation 2, with the second-order accurate stencil of Boore (1972). Alternatively, Hustedt et al. (2004) proposed to discretize first the first-order velocity-pressure system, equation 1, with second-order staggered-grid stencils (Yee; 1966; Virieux; 1986; Saenger et al.; 2000) and, second, to

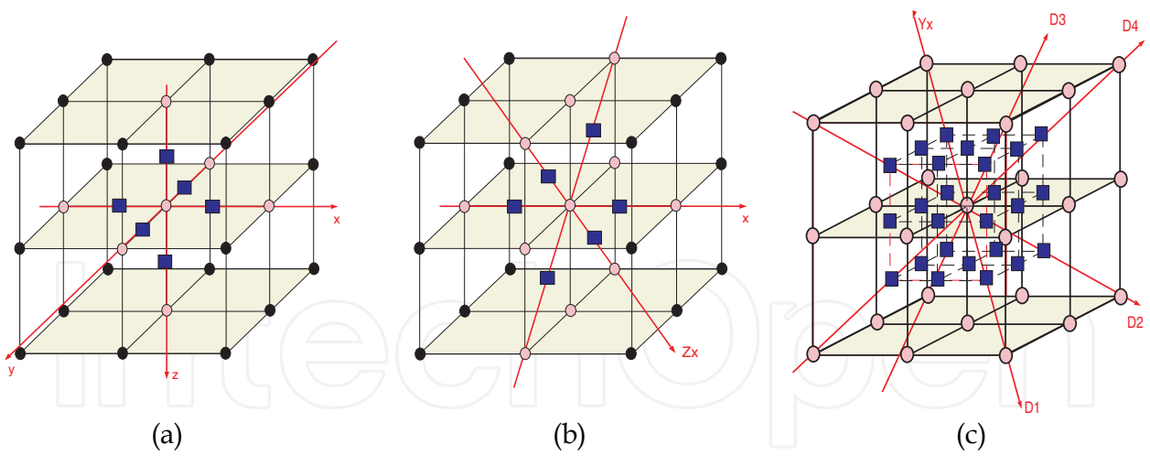

(a) (b) (c)

Fig. 1. Elementary FD stencils of the 3D mixed-grid stencil. Circles are pressure grid points. Squares are positions where buoyancy needs to be interpolated in virtue of the staggered-grid geometry. Gray circles are pressure grid points involved in the stencil. a) Stencil on the classic Cartesian coordinate system. This stencil incorporates 7 coefficients. b) Stencil on the rotated Cartesian coordinate system. Rotation is applied around x on the figure. This stencil incorporates 11 coefficients. Same strategy can be applied by rotation around y and z. Averaging of the 3 resultant stencils defines a 19-coefficient stencil. c) Stencil obtained from 4 coordinate systems, each of them being associated with 3 main diagonals of a cubic cell. This stencil incorporates 27 coefficients (Operto et al.; 2007).

eliminate the auxiliary wavefields (i.e., the velocity wavefields) following a parsimonious staggered-grid method originally developed in the time domain (Luo & Schuster; 1990). The parsimonious staggered-grid strategy allows us to minimize the number of wavefield components involved in the equation 4, and therefore to minimize the size of the system to be solved while taking advantage of the flexibility of the staggered-grid method to discretize first-order difference operators. The parsimonious mixed-grid approach originally proposed by Hustedt et al. (2004) for the 2D acoustic wave equation was extended to the 3D wave equation by Operto et al. (2007) and to a 2D pseudo-acoustic wave equation for transversely isotropic media with tilted symmetry axis by Operto et al. (2009). The staggered-grid method requires interpolation of the buoyancy in the middle of the FD cell which should be performed by volume harmonic averaging (Moczo et al.; 2002).
The pattern of the impedance matrix inferred from the 3D mixed-grid stencil is shown in Figure 2. The bandwidth of the matrix is of the order of N^2 (N denotes the dimension of a 3D cubic N^3 domain) and was kept minimal thanks to the use of low-order accurate stencils.

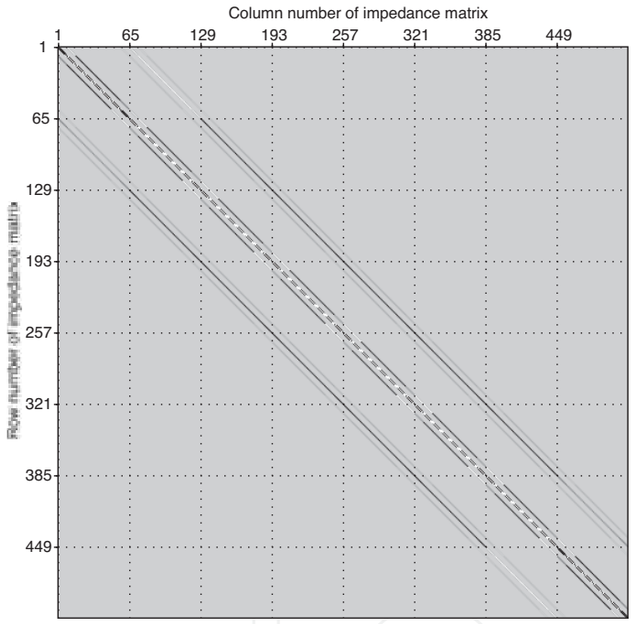

Fig. 2. Pattern of the square impedance matrix discretized with the 27-point mixed-grid stencil (Operto et al.; 2007). The matrix is band diagonal with fringes. The bandwidth is $\mathcal{O}(2N_1N_2)$ where N_1 and N_2 are the two smallest dimensions of the 3D grid. The number of rows/columns in the matrix is $N_1 \times N_2 \times N_3$. In the figure, $N_1 = N_2 = N_3 = 8$

3.2 Anti-lumped mass

The linear combination of the rotated stencils in the mixed-grid approach is complemented by the distribution of the mass term ω^2/κ in equation 2 over the different nodes of the mixed-grid stencil to mitigate the numerical dispersion:

$$\frac{\omega^2}{\kappa_{000}} p_{000} \Rightarrow \omega^2 \left(w_{m1} \left[\frac{p}{\kappa} \right]_0 + w_{m2} \left[\frac{p}{\kappa} \right]_1 + w_{m3} \left[\frac{p}{\kappa} \right]_2 + w_{m4} \left[\frac{p}{\kappa} \right]_3 \right), \tag{9}$$

where

$$w_{m1} + \frac{w_{m2}}{6} + \frac{w_{m3}}{12} + \frac{w_{m4}}{8} = 1. \tag{10}$$

In equation 9, the different nodes of the 27-point stencils are labelled by indices *lmn* where $l,m,n \in \{-1, 0,1\}$ and 000 denotes the grid point in the middle of the stencil.
We used the notations

$$\left[\frac{p}{\kappa}\right]_0 = \frac{p_{000}}{\kappa_{000}},$$

$$\left[\frac{p}{\kappa}\right]_1 = \frac{p_{100}}{\kappa_{100}} + \frac{p_{010}}{\kappa_{010}} + \frac{p_{001}}{\kappa_{001}} + \frac{p_{-100}}{\kappa_{-100}} + \frac{p_{0-10}}{\kappa_{0-10}} + \frac{p_{00-1}}{\kappa_{00-1}},$$

$$\left[\frac{p}{\kappa}\right]_2 = \frac{p_{110}}{\kappa_{110}} + \frac{p_{011}}{\kappa_{011}} + \frac{p_{101}}{\kappa_{101}} + \frac{p_{-110}}{\kappa_{-110}} + \frac{p_{0-11}}{\kappa_{0-11}} + \frac{p_{-101}}{\kappa_{-101}} + \frac{p_{1-10}}{\kappa_{1-10}} + \frac{p_{01-1}}{\kappa_{01-1}} + \frac{p_{10-1}}{\kappa_{10-1}} + \frac{p_{-1-10}}{\kappa_{-1-10}} + \frac{p_{0-1-1}}{\kappa_{0-1-1}} + \frac{p_{-10-1}}{\kappa_{-10-1}},$$

$$\left[\frac{p}{\kappa}\right]_3 = \frac{p_{111}}{\kappa_{111}} + \frac{p_{-1-1-1}}{\kappa_{-1-1-1}} + \frac{p_{-111}}{\kappa_{-111}} + \frac{p_{1-11}}{\kappa_{1-11}} + \frac{p_{11-1}}{\kappa_{11-1}} + \frac{p_{-1-11}}{\kappa_{-1-11}} + \frac{p_{1-1-1}}{\kappa_{1-1-1}} + \frac{p_{-11-1}}{\kappa_{-11-1}}.$$

This anti-lumped mass strategy is opposite to mass lumping used in finite element methods to make the mass matrix diagonal. The anti-lumped mass approach, combined with the averaging of the rotated stencils, allows us to minimize efficiently the numerical dispersion and to achieve an accuracy representative of 4^{th}-order accurate stencil from a linear combination of 2^{nd}-order accurate stencils. The anti-lumped mass strategy introduces four additional weighting coefficients w_{m1}, w_{m2}, w_{m3} and w_{m4}, equations 9 and 10. The coefficients w_1, w_2, w_3, w_{m1}, w_{m2}, w_{m3} and w_{m4} are determined by minimization of the phase-velocity dispersion in infinite homogeneous medium. Alternatives FD methods for designing optimized FD stencils can be found in Holberg (1987); Takeuchi and Geller (2000).

3.3 Numerical dispersion and anisotropy

The dispersion analysis of the 3D mixed-grid stencil was already developed in details in Operto et al. (2007). We focus here on the sensitivity of the accuracy of the mixed-grid stencil to the choice of the weighting coefficients w_1, w_2, w_3, w_{m1}, w_{m2}, w_{m3}. We aim to design an accurate stencil for a discretization criterion of 4 grid points per minimum propagated wavelength. This criterion is driven by the spatial resolution of full waveform inversion, which is half a wavelength. To properly sample subsurface heterogeneities, the size of which is half a wavelength, four grid points per wavelength should be used according to Shannon's theorem.
Inserting the discrete expression of a plane wave propagating in a 3D infinite homogeneous medium of wave speed *c* and density equal to 1 in the wave equation discretized with the mixed-grid stencil gives for the normalized phase velocity (Operto et al.; 2007):

$$\tilde{v}_{ph} = \frac{G}{\sqrt{2J\pi}} \sqrt{w_1(3-C) + \frac{w_2}{3}(6-C-B) + \frac{2w_3}{4}(3-3A+B-C)}, \tag{11}$$

where $J = (w_{m1} + 2w_{m2}C + 4w_{m3}B + 8w_{m4}A)$ with

$$A = \cos a \cos b \cos c,$$
$$B = \cos a \cos b + \cos a \cos c + \cos b \cos c,$$
$$C = \cos a + \cos b + \cos c.$$

and $a = \frac{2\pi}{G}\cos\phi\cos\theta$; $b = \frac{2\pi}{G}\cos\phi\sin\theta$; $c = \frac{2\pi}{G}\sin\phi$. Here, the normalized phase velocity is the ratio between the numerical phase velocity ω/k and the wave speed c. $G = \frac{\lambda}{h} = \frac{2\pi}{kh}$ is the number of grid points per wavelength λ. ϕ and θ are the incidence angles of the plane wave. We look for the 5 independent parameters w_{m1}, w_{m2}, w_{m3}, w_1, w_2 which minimize the least-squares norm of the misfit $(1. - \tilde{v}_{ph})$. The two remaining weighting coefficients w_{m4} and w_3 are inferred from equations 8 and 10, respectively. We estimated these coefficients by a global optimization procedure based on a Very Fast Simulating Annealing algorithm (Sen & Stoffa; 1995). We minimize the cost function for 5 angles ϕ and θ spanning between 0 and 45°and for different values of G.

In the following, the number of grid points for which phase velocity dispersion is minimized will be denoted by G_m. The values of the weighting coefficients as a function of G_m are given in Table 1. For high values of G_m, the Cartesian stencil has a dominant contribution (highlighted by the value of w_1), while the first rotated stencil has the dominant contribution for low values of G_m as shown by the value of w_2. The dominant contribution of the Cartesian stencil for large values of G_m is consistent with the fact that it has a smaller spatial support (i.e., $2 \times h$) than the rotated stencils and a good accuracy for G greater than 10 (Virieux; 1986). The error on the phase velocity is plotted in polar coordinates for four values of G (4, 6, 8, 10) and for G_m=4 in Figure 3a. We first show that the phase velocity dispersion is negligible for G=4, that shows the efficiency of the optimization. However, more significant error (0.4 %) is obtained for intermediate values of G (for example, G=6 in Figure 3a). This highlights the fact that the weighting coefficients were optimally designed to minimize the dispersion for one grid interval in homogeneous media. We show also the good isotropy properties of the stencil, shown by the rather constant phase-velocity error whatever the direction of propagation. The significant phase-velocity error for values of G greater than G_m prompt us to simultaneously minimize the phase-velocity dispersion for four values of G: G_m= 4,6,8,10 (Figure 3b). We show that the phase-velocity error is now more uniform over the values of G and that the maximum phase-velocity-error was reduced (0.25 % against 0.4 %). However, the nice isotropic property of the mixed-grid stencil was degraded and the phase-velocity dispersion was significantly increased for G=4. We conclude that the range of wavelengths propagated in a given medium should drive the discretization criterion used to infer the weighting coefficients of the mixed grid stencil and that a suitable trade-off should be found between the need to manage the heterogeneity of the medium and the need to minimize the error for a particular wavelength. Of note, an optimal strategy might consist of adapting locally the values of the weighting coefficients to the local wave speed during the assembling of the impedance matrix. This strategy was not investigated yet.

G_m	4,6,8,10	4	8	10	20	40
wm_1	0.4966390	0.5915900	0.5750648	0.7489436	0.7948160	0.6244839
wm_2	7.51233E-02	4.96534E-02	5.76759E-02	1.39044E-02	3.71392E-03	5.06646E-02
wm_3	4.38464E-03	5.10851E-03	5.56914E-03	6.38921E-03	5.54043E-03	1.42369E-03
wm_4	6.76140E-07	6.14837E-03	1.50627E-03	1.13699E-02	1.45519E-02	6.8055E-03
w_1	5.02480E-05	8.8075E-02	0.133953	0.163825	0.546804	0.479173
w_2	0.8900359	0.8266806	0.7772883	0.7665769	0.1784437	0.2779923
w_3	0.1099138	8.524394E-02	8.87589E-02	6.95979E-02	0.2747527	0.2428351

Table 1. Coefficients of the mixed-grid stencil as a function of the discretization criterion G_m for the minimization of the phase velocity dispersion.

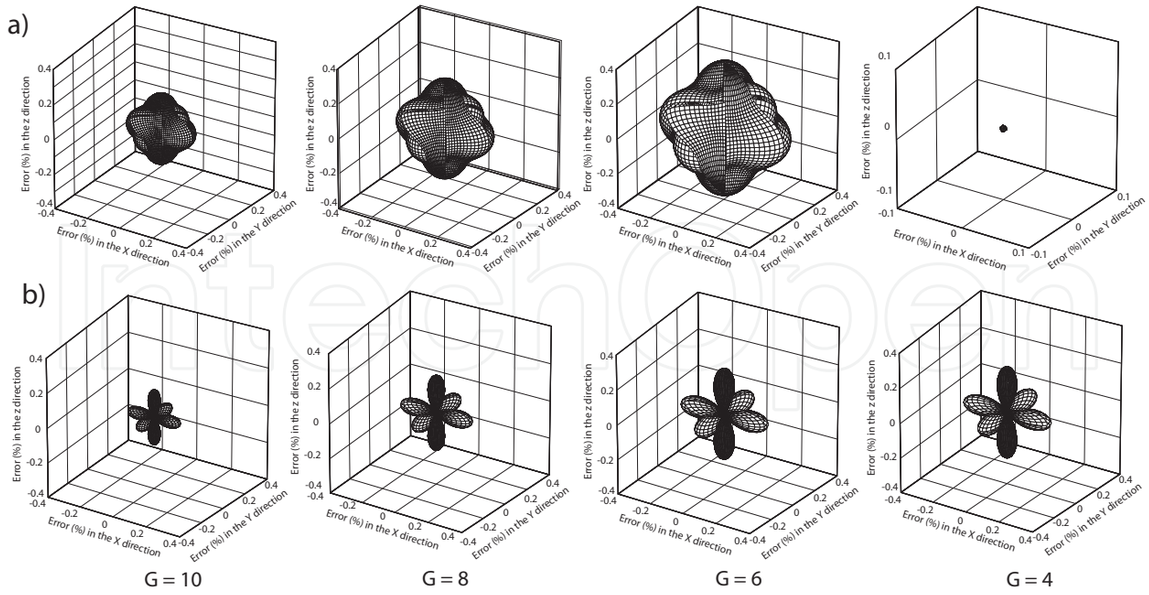

Fig. 3. Phase-velocity dispersion shown in spherical coordinates for four values of G. (a) The phase-velocity dispersion was minimized for G = 4. (b) the phase-velocity dispersion was minimized for 4 values of G: 4, 6, 8 and 10.

Comparison between numerical and analytical pressure monochromatic wavefields computed in a homogeneous medium of wave speed 1.5 km/s and density 1000 kg/m^3 confirms the former theoretical analysis (Figure 4). The frequency is 3.75 Hz corresponding to a propagated wavelength of 400 m. The grid interval for the simulation is 100 m corresponding to G = 4. Simulations were performed when the weighting coefficients of the mixed-grid stencils are computed for G_m = 4 and G_m = {4, 6, 8,10}. The best agreement is obtained for the weighting coefficients associated with G_m = 4 as expected from the dispersion analysis.

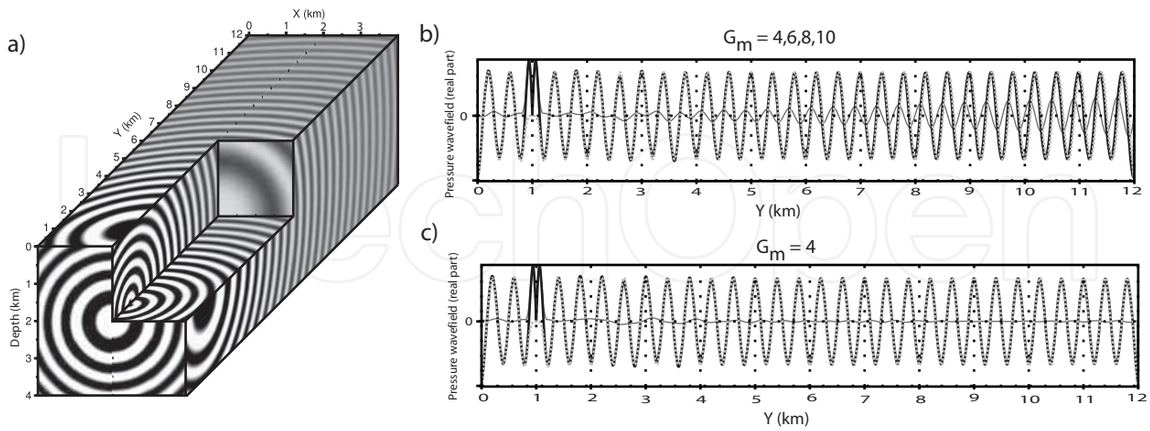

Fig. 4. (a) Real part of a 3.75-Hz monochromatic wavefield computed with the mixed-grid stencil in a 3D infinite homogeneous medium. The explosive point source is at x=2 km, y=1 km, z=2 km. (b-c) Comparison between the analytical (gray) and the numerical solution (black) for a receiver line oriented in the *Y* direction across the source position. The thin black line is the difference. The amplitudes were corrected for 3D geometrical spreading. (b) G_m = 4, 6, 8, 10. (c) G_m = 4.

3.4 Boundary conditions

In seismic exploration, two boundary conditions are implemented for wave modelling: absorbing boundary conditions to mimic an infinite medium and free surface conditions on the top side of the computational domain to represent the air-solid or air-water interfaces.

3.4.1 PML absorbing boundary conditions

We use Perfectly-Matched Layers (PML) absorbing boundary conditions (Berenger; 1994) to mimic an infinite medium. In the frequency domain, implementation of PMLs consists of applying in the wave equation a new system of complex-valued coordinates $\tilde{x}$ defined by (e.g., Chew & Weedon; 1994):

$$\frac{\partial}{\partial \tilde{x}} = \frac{1.}{\xi_x(x)} \frac{\partial}{\partial x} \tag{12}$$

In the PML layers, the damped wave equation writes:

$$\left[\frac{\omega^2}{\kappa(\mathbf{x})} + \frac{1}{\xi_x(x)} \frac{\partial}{\partial x} \frac{b(\mathbf{x})}{\xi_x(x)} \frac{\partial}{\partial x} + \frac{1}{\xi_y(y)} \frac{\partial}{\partial y} \frac{b(\mathbf{x})}{\xi_y(y)} \frac{\partial}{\partial y} + \frac{1}{\xi_z(z)} \frac{\partial}{\partial z} \frac{b(\mathbf{x})}{\xi_z(z)} \frac{\partial}{\partial z} \right] p(\mathbf{x}, \omega) = -s(\mathbf{x}, \omega), \tag{13}$$

where $\xi_x(x) = 1 + i\gamma_x(x)/\omega$ and $\gamma_x(x)$ is a 1D damping function which defines the PML damping behavior in the PML layers. These functions differ from zero only inside the PML layers. In the PML layers, we used $\gamma(x) = c_{pml}\left(1 - cos(\frac{\pi}{2}\frac{L-x}{L})\right)$ where L denotes the width of the PML layer and x is a local coordinate in the PML layer whose origin is located at the outer edges of the model. The scalar c_{pml} is defined by trial and error depending on the width of the PML layer. The procedure to derive the unsplitted second-order wave equation with PML conditions, equation 13, from the first-order damped wave equation is given in Operto et al. (2007).

The absorption of the PML layers at grazing incidence can be improved by using convolutional PML (C-PML) (Kuzuoglu & Mittra; 1996; Roden & Gedney; 2000; Komatitsch & Martin; 2007). In the C-PML layers, the damping function $\xi_x(x)$ becomes:

$$\xi_x(x) = \kappa_x + i\frac{d_x}{\alpha_x + i\omega}, \tag{14}$$

where d_x and α_x are generally quadratic and linear functions, respectively. Suitable expression for κ_x, d_x and α_x are discussed in Kuzuoglu & Mittra (1996); Collino & Monk (1998); Roden & Gedney (2000); Collino & Tsogka (2001); Komatitsch & Martin (2007); Drossaert & Giannopoulos (2007).

3.4.2 Free surface boundary conditions

Planar free surface boundary conditions can be simply implemented in the frequency domain with two approaches. In the first approach, the free surface matches the top side of the FD grid and the pressure is forced to zero on the free surface by using a diagonal impedance matrix for rows associated with collocation grid points located on the top side of the FD grid. Alternatively, the method of image can be used to implement the free surface along a virtual plane located half a grid interval above the topside of the FD grid (Virieux;

1986). The pressure is forced to vanish at the free surface by using a ficticious plane located half a grid interval above the free surface where the pressure is forced to have opposite values to that located just below the free surface.
From a computer implementation point of view, an impedance matrix is typically built row per row. One row of the linear system can be written as:

$$\sum_{i_3=-1,1}\sum_{i_2=-1,1}\sum_{i_1=-1,1} a_{i_1 i_2 i_3}\, p_{i_1 i_2 i_3} = s_{000} \tag{15}$$

where $a_{i_1 i_2 i_3}$ are the coefficients of the 27-point mixed grid stencil and 000 denote the indices of the collocation coefficient located in the middle of the stencil in a local coordinate system. The free surface boundary conditions writes:

$$p_{-1 i_2 i_3} = -p_{0 i_2 i_3}, \tag{16}$$

for $i_2 = \{-1, 0,1\}$ and $i_3 = \{-1, 0,1\}$. The indices i_1=-1 and i_1=0 denotes here the grid points just above and below the free surface, respectively.
For a grid point located on the top side of the computational domain (i.e., half a grid interval below free surface), equation 15 becomes:

$$\sum_{i_3=-1,1}\sum_{i_2=-1,1} a_{1 i_2 i_3}\, p_{1 i_2 i_3} + \sum_{i_3=-1,1}\sum_{i_2=-1,1} \left(a_{0 i_2 i_3} - a_{-1 i_2 i_3}\right) p_{0 i_2 i_3} = s_{000}, \tag{17}$$

where $p_{-1 i_2 i_3}$ has been replaced by the opposite value of $p_{0 i_2 i_3}$ according to equation 16.
Our practical experience is that both implementation of free surface boundary conditions give results of comparable accuracy. Of note, rigid boundary conditions (zero displacement perpendicular to the boundary) or periodic boundary conditions (Ben-Hadj-Ali et al.; 2008) can be easily implemented with the method of image following the same principle than for the free surface condition.

3.5 Source implementation on coarse grids

Seismic imaging by full waveform inversion is initiated at frequency as small as possible to mitigate the non linearity of the inverse problem. The starting frequency for modelling can be as small as 2 Hz which can lead to grid intervals as large as 200 m. In this framework, accurate implementation of point source at arbitrary position in a coarse grid is critical. One method has been proposed by Hicks (2002) where the point source is approximated by a windowed Sinc function. The Sinc function is defined by

$$sinc(x) = \frac{sin(\pi x)}{\pi x}, \tag{18}$$

where $x = (x_g - x_s)$, x_g denotes the position of the grid nodes and x_s denotes the position of the source. The Sinc function is tapered with a Kaiser function to limit its spatial support. For multidimensional simulations, the interpolation function is built by tensor product construction of 1D windowed Sinc functions. If the source positions matches the position of one grid node, the Sinc function reduces to a Dirac function at the source position and no approximation is used for the source positioning. If the spatial support of the Sinc function

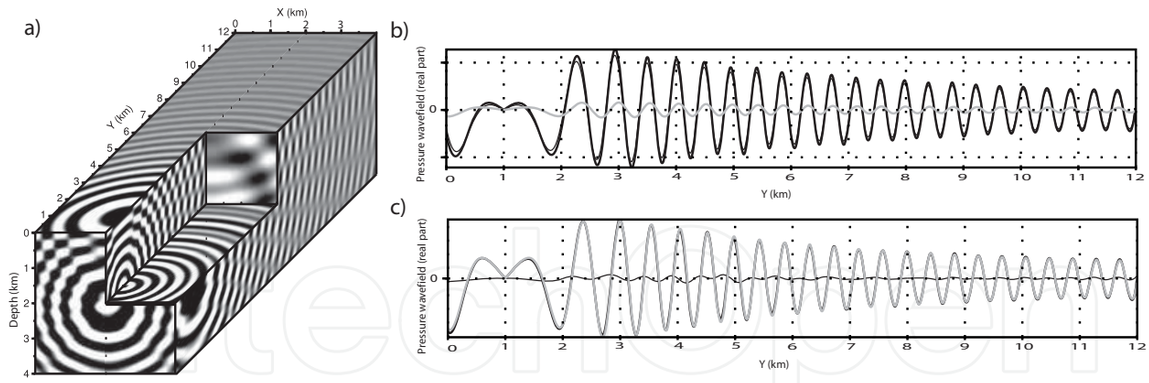

Fig. 5. a) Real part of a 3.75-Hz monochromatic wavefield in a homogeneous half space. (b) Comparison between numerical (black) and analytical (gray) solutions at receiver positions. The Sinc interpolation with 4 coefficients was used for both the source implementation and the extraction of the solution at the receiver positions on a coarse FD grid.

intersects a free surface, part of the Sinc function located above the free surface is mirrored into the computational domain with a reverse sign following the method of image. Vertical force can be implemented in a straightforward way by replacing the Sinc function by its vertical derivative. The same interpolation function can be used for the extraction of the pressure wavefield at arbitrary receiver positions. The accuracy of the method of Hicks (2002) is illustrated in Figure 5 which shows a 3.5-Hz monochromatic wavefield computed in a homogeneous half space. The wave speed is 1.5 km/s and the density is 1000 kg/m^3. The grid interval is 100 m. The free surface is half a grid interval above the top of the FD grid and the method of image is used to implement the free surface boundary condition. The source is in the middle of the FD cell at 2 km depth. The receiver line is oriented in the *Y* direction. Receivers are in the middle of the FD cell in the horizontal plane and at a depth of 6 m just below the free surface. This setting is representative of a ocean bottom survey where the receiver is on the sea floor and the source is just below the sea surface (in virtue of the spatial reciprocity of the Green functions, sources are processed here as receivers and *vice versa*). Comparison between the numerical and the analytical solutions at the receiver positions are first shown when the source is positioned at the closest grid point and the numerical solutions are extracted at the closest grid point (Figure 5b). The amplitude of the numerical solution is strongly overestimated because the numerical solution is extracted at a depth of 50 m below free surface (where the pressure vanishes) instead of 6 m. Second, a significant phase shift between numerical and analytical solutions results from the approximate positioning of the sources and receivers. In contrast, a good agreement between the numerical and analytical solutions both in terms of amplitude and phase is shown in Figure 5c where the source and receiver positioning were implemented with the windowed Sinc interpolation.

3.6 Resolution with the sparse direct solver MUMPS

To solve the sparse system of linear equations, equation 4, we used the massively parallel direct MUMPS solver designed for distributed memory platforms. The reader is referred to Guermouche et al. (2003); Amestoy et al. (2006); MUMPS team (2009) for an extensive description of the method and their underlying algorithmic aspects. The MUMPS solver is based on a multifrontal method (Duff et al.; 1986; Duff and Reid; 1983; Liu; 1992), where the

resolution of the linear system is subdivided into 3 main tasks. The first one is an analysis phase or symbolic factorization. Reordering of the matrix coefficients is first performed in order to minimize fill-in. We used the METIS algorithm which is based on a hybrid multilevel nested-dissection and multiple minimum degree algorithm (Karypis & Kumar; 1999). Then, the dependency graph which describes the order in which the matrix can be factored is estimated as well as the memory required to perform the subsequent numerical factorization. The second task is the numerical factorization. The third task is the solution phase performed by forward and backward substitutions. During the solution phase, multiple-shot solutions can be computed simultaneously from the LU factors taking advantage of threaded BLAS3 (Basic Linear Algebra Subprograms) library and are either assembled on the host or kept distributed on the processors for subsequent parallel computations.

We performed the factorization and the solutions phases in complex arithmetic single precision. To reduce the condition number of the matrix, a row and column scaling is applied in MUMPS before factorization. The sparsity of the matrix and suitable equilibration have made single precision factorization accurate enough so far for the 2D and 3D problems we tackled. If single precision factorization would be considered not accurate enough for very large problems, an alternative approach to double precision factorization may be the postprocessing of the solution by a simple and fast iterative refinement performed in double precision (Demmel (1997), pages 60-61 and Langou et al. (2006); Kurzak & Dongarra (2006)).

The main two bottlenecks of sparse direct solver is the time and memory complexity and the limited scalability of the LU decomposition. By complexity is meant the increase of the computational cost (either in terms of elapsed time or memory) of an algorithm with the size of the problem, while scalability describes the ability of a given algorithm to use an increasing number of processors. The theoretical memory and time complexity of the LU decomposition for a sparse matrix, the pattern of which is shown in Figure 2, is $\mathcal{O}(N^4)$ and $\mathcal{O}(N^6)$, respectively, where N is the dimension of a 3D cubic N^3 grid.

We estimated the observed memory complexity and scalability of the LU factorization by means of numerical experience. The simulations were performed on the SGI ALTIX ICE supercomputer of the computer center CINES (France). Nodes are composed of two quad-core INTEL processors E5472. Each node has 30 Gbytes of useful memory. We used two MPI process per node and four threads per MPI process. In order to estimate the memory complexity, we performed simulations on cubic models of increasing dimension with PML absorbing boundary conditions along the 6 sides of the model. The medium is homogeneous and the source is on the middle of the grid. Figure 6a shows the memory required to store the complex-valued LU factors as a function of N. Normalization of this curve by the real memory complexity will lead to a horizontal line. We found an observed memory complexity of $\mathcal{O}(Log_2(N)N^{3.9})$ (Figure 6b) which is consistent with the theoretical one. In order to assess the scalability of the LU factorization, we consider a computational FD grid of dimensions 177 x 107 x 62 corresponding to 1.17 millions of unknowns. The size of the grid corresponds to a real subsurface target for oil exploration at low frequency (3.5 Hz). We computed a series of LU factorization using an increasing number of processors N_p, starting with $N_{p_{ref}} = 2$. The elapsed time of the LU factorization (T_{LU}) and the parallelism efficiency ($T_{LU}(N_{p_{ref}}) \times N_{p_{ref}} / T_{LU}(N_p) \times N_p$) are shown in Figure 6(c-d). The efficiency drops rapidly as the number of processors increased, down to a value of 0.5 for $N_P = 32$ (Figure 6d). This clearly indicates that the most suitable platform for sparse direct solver should be composed

of a limited number of nodes with a large amount of shared memory. The efficiency of the multi-r.h.s solution phase is significantly improved by using multithreaded BLAS3 library.

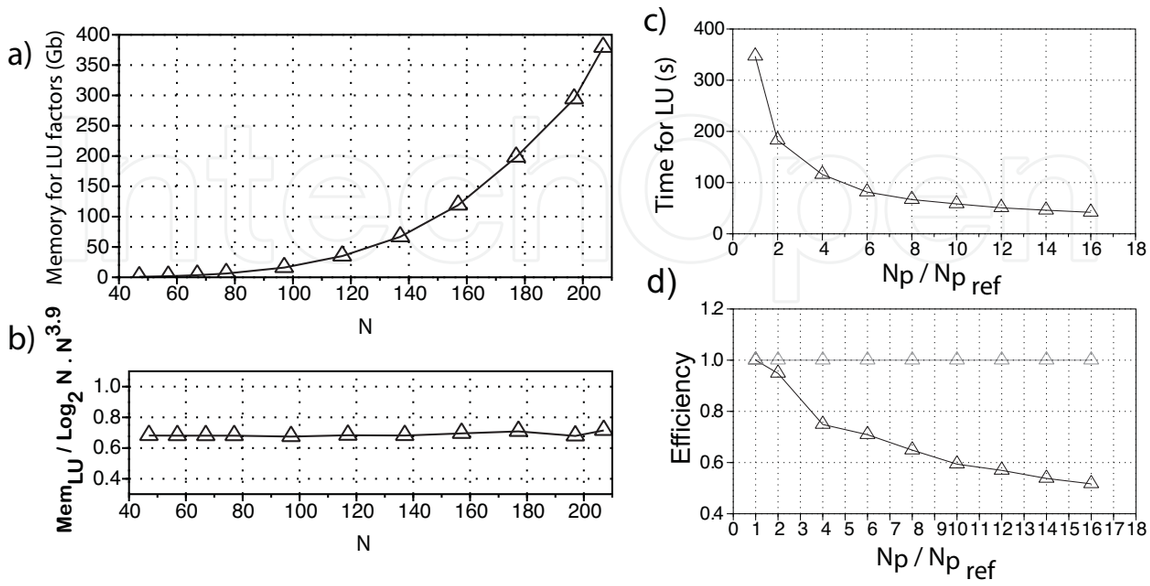

Fig. 6. (a-b) Memory complexity of LU factorization. (a) Memory in Gbytes required for storage of LU factors. (b) Memory required for storage of LU factors divided by $Log_2 N.N^{3.9}$. N denotes the dimension of a 3D N^3 grid. The largest simulation for N = 207 corresponds to 8.87 millions of unknowns. (c-d) Scalability analysis of LU factorization. (c) Elapsed time for LU factorization versus the number of MPI processes. (d) Efficiency.

3.7 Numerical examples

We present acoustic wave modelling in two realistic 3D synthetic velocity models, the SEG/EAGE overthrust and salt models, developed by the oil exploration community to assess seismic modelling and imaging methods (Aminzadeh et al.; 1997). The simulation was performed on the SGI ALTIX ICE supercomputer just described.

3.7.1 3D EAGE/SEG overthrust model

The 3D SEG/EAGE Overthrust model is a constant density onshore acoustic model covering an area of 20 km × 20 km × 4.65 km (Aminzadeh et al.; 1997)(Figure 7a). From a geological viewpoint, it represents a complex thrusted sedimentary succession constructed on top of a structurally decoupled extensional and rift basement block. The overthrust model is discretized with 25 m cubic cells, representing an uniform mesh of 801 × 801 × 187 nodes. The minimum and maximum velocities in the Overthrust model are 2.2 and 6.0 km/s respectively. We present the results of a simulation performed with the mixed-grid FD method (referred to as FDFD in the following) for a frequency of 7 Hz and for a source located at x=2.4 km, y=2.4 km and z=0.15 km. The model was resampled with a grid interval of 75 m that corresponds to four grid points per minimum wavelength. The size of the resampled FD grid is 266 x 266 x 62. PML layers of 8 grid points were added along the 6 sides of the 3D FD grid. This leads to 6.2 millions of pressure unknowns. For the simulation,

we used the weights of the mixed-grid stencil obtained for G_m = 4, 6, 8, 10. These weights provided slightly more accurate results than the weights obtained for G_m = 4, in particular for waves recorded at long source-receiver offsets. The 7-Hz monochromatic wavefield computed with the FDFD method is compared with that computed with a classic $\mathcal{O}(\Delta t^2,\Delta x^4)$ staggered-grid FD time-domain (FDTD) method where the monochromatic wavefield is integrated by discrete Fourier transform within the loop over time steps (Sirgue et al.; 2008) (Figure 7).

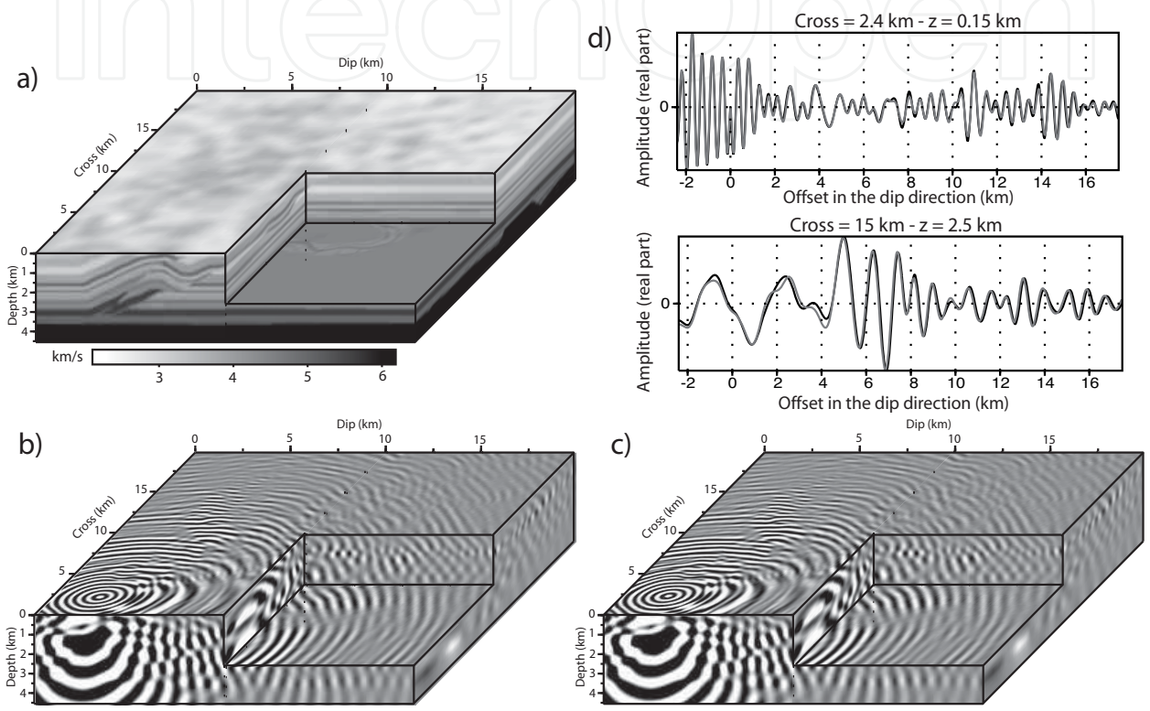

Fig. 7. (a) Overthrust velocity model. (b-c) 7-Hz monochromatic wavefield (real part) computed with the FDFD (b) and FDTD (c) methods.(d) Direct comparison between FDFD (gray) and FDTD (black) solutions. The receiver line in the dip direction is: (top) at 0.15-km depth and at 2.4 km in the cross direction. The amplitudes were corrected for 3D geometrical spreading; (bottom) at 2.5-km depth and at 15 km in the cross direction.

We used the same spatial FD grid for the FDTD and FDFD simulations. The simulation length was 15 s in the FDTD modelling. We obtain a good agreement between the two solutions (Figure 7d). The statistics of the FDFD and FDTD simulations are outlined in Table 2. The FDFD simulation was performed on 32 MPI processes with 2 threads and 15 Gbytes of memory per MPI process. The total memory required by the LU decomposition of the impedance matrix was 260 Gbytes. The elapsed time for LU decomposition was 1822 s and the elapsed time for one r.h.s was 0.97 s. Of note, we processed efficiently groups of 16 sources in parallel during the solution step by taking advantage of the multi-rhs functionality of MUMPS and the threaded BLAS3 library. The elapsed time for the FDTD simulation was 352 s on 4 processors. Of note, C-PML absorbing boundary conditions were implemented in the full model during FDTD modelling to mimic attenuation effects

Model	F (Hz)	h(m)	n_u (10^6)	$M_{LU}(Gb)$	$T_{LU}(s)$	$T_s(s)$	N_p^{fdfd}	N_P^{fdtd}	$T_{fdtd}(s)$
Over.	7	75	6.2	260	1822	0.97	32	4	352
Salt	7.34	50	8.18	402.5	2863	1.4	48	16	211

Table 2. Statistics of the simulation in the overthrust (top row) and in the salt (bottom row) models. $F(Hz)$: frequency; $h(m)$: FD grid interval; n_u: number of unknowns; M_{LU}: memory used for LU factorization in Gbytes; T_{LU}: elapsed time for factorization; T_s: elapsed time for one solution phase; N_p^{fdfd} : number of MPI processors used for FDFD; N_p^{fdtd} : number of MPI processors used for FDTD; T_{fdtd}: elapsed time for one FDTD simulation.

Model	Method	Pre. (hr)	Sol. (hr)	Total (hr)	Pre. (hr)	Sol. (hr)	Total (hr)
Over.	FDTD	0	21.7	21.7	0	0.96	0.96
Over.	FDFD	0.5	0.54	1.04	0.5	0.0134	0.51
Salt	FDTD	0	39	39	0	0.94	0.94
Salt	FDFD	0.8	0.78	1.58	0.80	0.016	0.816

Table 3. Comparison between FDTD and FDFD modelling for 32 (left) and 2000 (right) processors. The number of sources is 2000. *Pre*. denotes the elapsed time for the source-independent task during seismic modelling (i.e., the LU factorization in the FDFD approach). *Sol*. Denotes the elapsed time for multi-r.h.s solutions during seismic modelling (i.e., the substitutions in the FDFD approach).

implemented with memory variables. To highlight the benefit of the direct-solver approach for multi-r.h.s simulation on a small number of processors, we compare the performances of the FDFD and FDTD simulations for 2000 sources (Table 3). If the number of available processors is 32, the FDFD method is more than one order of magnitude faster than the FDTD one thanks of the efficiency of the solution step of the direct-solver approach. If the number of processors equals to the number of sources, the most efficient parallelization of the FDTD method consists of assigning one source to one processor and performing the FDTD simulation in sequential on each processor. For a large number of processors, the cost of the FDFD method is dominated by the LU decomposition (if the 2000 processors are splitted into groups of 32 processors, each group being assigned to the processing of 2000/32 sources) and the computational cost of the two methods is of the same order of magnitude. This schematic analysis highlights the benefit of the FDFD method based on sparse direct solver to tackle efficiently problems involving few millions of unknowns and few thousands of r.h.s on small distributed-memory platforms composed of nodes with a large amount of shared memory.

3.7.2 3D EAGE/SEG salt model

The salt model is a constant density acoustic model covering an area of 13.5 km × 13.5 km × 4.2 km (Aminzadeh et al.; 1997)(Figure 8). The salt model is representative of a Gulf Coast salt structure which contains salt sill, different faults, sand bodies and lenses. The salt model is discretized with 20 m cubic cells, representing an uniform mesh of 676 x 676 x 210 nodes. The minimum and maximum velocities in the salt model are 1.5 and 4.482 km/s respectively. We performed a simulation for a frequency of 7.34 Hz and for one source located at x=3.6 km, y=3.6 km and z = 0.1 km. The model was resampled with a grid interval of 50 m corresponding to 4 grid points per minimum wavelength. The dimension of the

resampled grid is 270 x 270 x 84 which represents 8.18 millions of unknowns after addition of the PML layers. We used the weights of the mixed-grid stencil inferred from G_m = 4, 6, 8, 10. Results of simulations performed with the FDFD and FDTD methods are compared in Figure 8. The length of the FDTD simulation was 15 s.

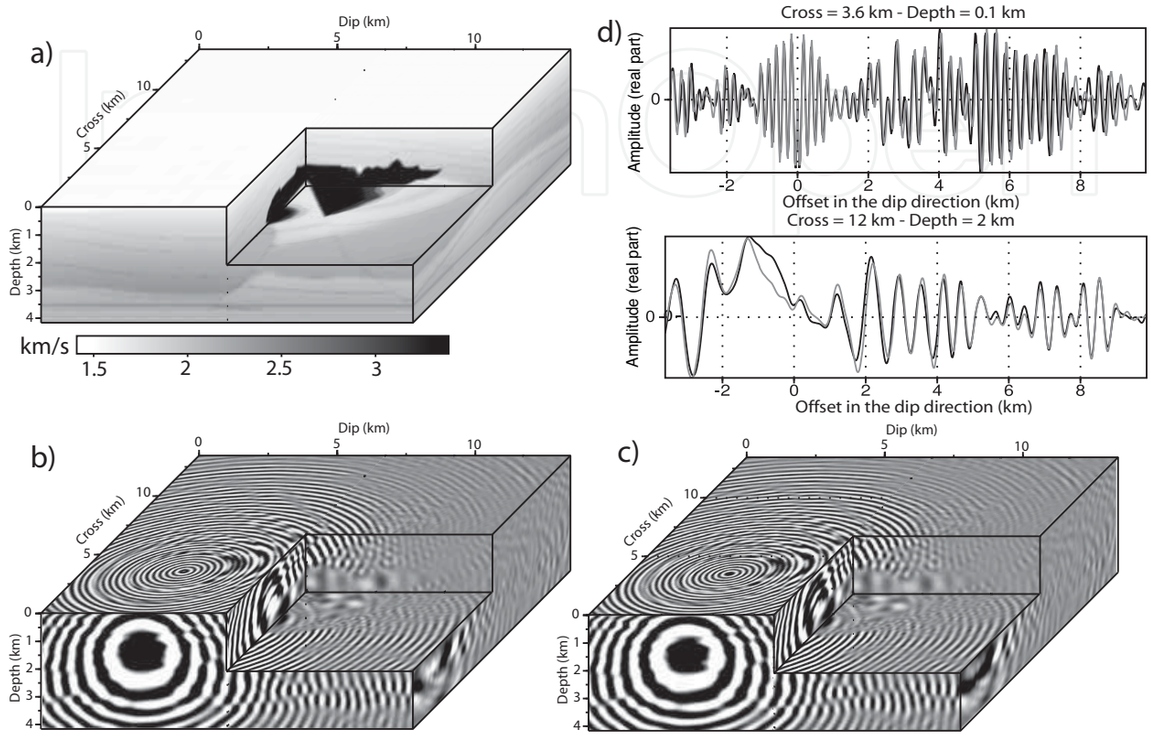

Fig. 8. (a) Salt velocity model. (b-c) 7.33-Hz monochromatic wavefield (real part) computed with the FDFD (b) and the FDTD (c) methods. (d) Direct comparison between FDFD (gray) and FDTD (black) solutions. The receiver line in the dip direction is: (top) at 0.1-km depth and at 3.6 km in the cross direction. The amplitudes were corrected for 3D geometrical spreading. (bottom) at 2.5-km depth and at 15 km in the cross direction.

The statistics of the simulation are outlined in Table 2. We obtain a good agreement between the two solutions (Figure 8d) although we show a small phase shift between the two solutions at offsets greater than 5 km. This phase shift results from the propagation in the high-velocity salt body. This phase shift is higher when the FDFD is performed with weights inferred from G_m = 4. The direct-solver modelling was performed on 48 MPI process using 2 threads and 15 Gbytes of memory per MPI process. The memory and the elapsed time for the LU decomposition were 402 Gbytes and 2863 s, respectively. The elapsed time for the solution step for one r.h.s was 1.4 s when we process 16 rhs at a time during the solution step in MUMPS. The elapsed time for one FDTD simulation on 16 processors was 211 s. As for the overthrust model, the FDFD approach is more than one order of magnitude faster than the FDTD one when a large number of r.h.s (2000) and a small number of processors (48) are used (Table 3). For a number of processors equal to the number of r.h.s, the two approaches have the same cost. Of note, in the latter configuration (N_P=N_{rhs}), the cost of the FDFD modelling and of the FDTD modelling are almost equal in the case of the salt model (0.94 h versus 0.816 h) while the FDFD modelling was almost two times faster in the case of

the smaller overthrust case study (0.96 h versus 0.51 h). This trend simply highlights the higher scalability of the FDTD method.

4. Finite-element Discontinuous Galerkin method in the frequency domain

We just presented applications of the FD frequency-domain method in weakly-contrasted media with flat topography where the FD where the FD method is expected to perform well. However, in land exploration seismology, there is a need to perform elastic wave modelling in area of complex topography such as foothills and thrust belts (Figure 9). Moreover, onshore targets often exhibit weathered layers with very low wave speeds in the near surface which require a locally-refined discretization for accurate modelling. In shallow water environment, a mesh refinement is also often required near the sea floor for accurate modelling of guided and interface waves near the sea floor. Accurate modelling of acoustic and elastic waves in presence of complex boundaries of arbitrary shape and the local adaptation of the discretization to local features such as weathered near surface layers or sea floor were two of our motivations behind the development of a discontinuous finite element method on unstructured meshes for acoustic and elastic wave modelling.

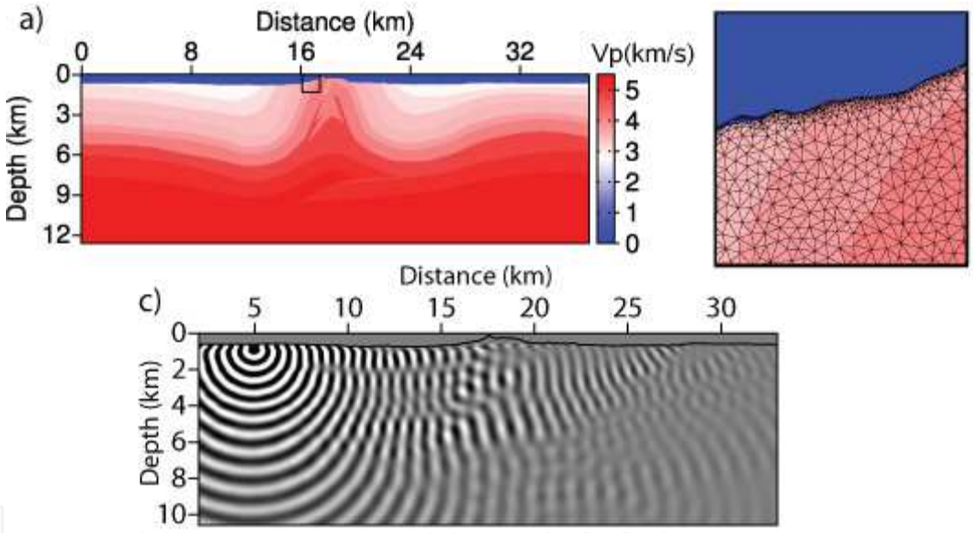

Fig. 9. Application of the DG method in seismic exploration. (a) Velocity model representative of a foothill area affected by a hilly relief and a weathered layer in the near surface. (b) Close-up of the unstructured triangular mesh locally refined near the surface. (c) Example of monochromatic pressure wavefield.

4.1 *hp*-adaptive Discontinuous Galerkin discretization

In the finite-element framework, the wavefields are approximated by means of local polynomial basis functions defined in volume elements. In the following, we adopt the nodal form of the DG formulation, assuming that the wavefield vector is approximated in triangular or tetrahedral elements for 2D and 3D problems, respectively:

$$\vec{u}_i(\omega,x,y,z,t) = \sum_{j=1}^{d_i} \vec{u}_{ij}(\omega,x_j,y_j,z_j)\varphi_{ij}(\omega,x,y,z), \tag{19}$$

where $\vec{u}$ is the wavefield vector of components $\vec{u}$ = (p,v_x,v_y,v_z). i is the index of the element in an unstructured mesh. $\vec{u}_i$ (ω,x,y,z) denotes the wavefield vector in the element i and (x,y,z) are the coordinates inside the element i. In the framework of the nodal form of the DG method, φ_{ij} denotes Lagrange polynomial and d_i is the number of nodes in the element i. The position of the node j in the element i is denoted by the local coordinates (x_j,y_j,z_j).
In the following, the first-order acoustic velocity-pressure system, equation 1, will be written in a pseudo-conservative form:

$$\mathcal{M}\vec{u} = \sum_{\theta\in\{x,y,z\}} \partial_\theta \left(\mathcal{N}_\theta \vec{u}\right) + \vec{s}, \tag{20}$$

where

$$\mathcal{M} = \begin{pmatrix} -i\omega/\kappa & 0 & 0 & 0 \\ 0 & -i\omega\rho & 0 & 0 \\ 0 & 0 & -i\omega\rho & 0 \\ 0 & 0 & 0 & -i\omega\rho \end{pmatrix} \tag{21}$$

$$\mathcal{N}_x = \begin{pmatrix} 0 & 1 & 0 & 0 \\ 1 & 0 & 0 & 0 \\ 0 & 0 & 0 & 0 \\ 0 & 0 & 0 & 0 \end{pmatrix} \quad \mathcal{N}_y = \begin{pmatrix} 0 & 0 & 1 & 0 \\ 0 & 0 & 0 & 0 \\ 1 & 0 & 0 & 0 \\ 0 & 0 & 0 & 0 \end{pmatrix} \quad \mathcal{N}_z = \begin{pmatrix} 0 & 0 & 0 & 1 \\ 0 & 0 & 0 & 0 \\ 0 & 0 & 0 & 0 \\ 1 & 0 & 0 & 0 \end{pmatrix}, \tag{22}$$

$\mathcal{N}_\theta \vec{u}$ are linear fluxes and $\vec{s}$ is the source vector.
The first step in the finite-element formulation is to obtain the weak form of the first-order acoustic velocity-stress system by multiplying equation 20 by a test function φ_{ir} and integration over the element volume V_i

$$\int_{V_i} \varphi_{ir} \mathcal{M}_i \vec{u}_i dV = \int_{V_i} \varphi_{ir} \sum_{\theta\in\{x,y,z\}} \partial_\theta \left(\mathcal{N}_\theta \vec{u}_i\right) dV + \int_{V_i} \varphi_{ir} \vec{s}_i dV, \tag{23}$$

where $r \in [1,d_i]$. In the framework of Galerkin methods, we used the same function for the test function and the shape function, equation 19.
Integration by parts of the right hand side of equation 23 leads to:

$$\int_{V_i} \varphi_{ir} \mathcal{M}\vec{u}_i dV = -\int_{V_i} \sum_{\theta\in\{x,y,z\}} \partial_\theta \varphi_{ir} \left(\mathcal{N}_\theta \vec{u}_i\right) dV + \int_{S_i} \varphi_{ir} \left(\sum_{\theta\in\{x,y,z\}} \mathcal{N}_\theta n_\theta \right) \vec{u}_i dS + \int_{V_i} \varphi_{ir} \vec{s}_i dV, \tag{24}$$

where S_i is the surface of the element i and $\vec{n}$ = (n_x,n_y,n_z) is the outward pointing unit normal vector with respect to the surface i. We recognize in the second term of the right-hand side of equation 24 the numerical flux $\mathbf{f}_i$ defined by:

$$\mathbf{n}\cdot\mathbf{f}_i = \sum_{\theta\in\{x,y,z\}} \mathcal{N}_\theta n_\theta \vec{u}_i \tag{25}$$

A suitable expression $\mathbf{f}_{i/k}$ of the numerical flux $\mathbf{f}_i$ should guarantee the consistency between the values of the wavefield computed at a node shared by two neighbor elements i and k.

In this study we used centered fluxes for their energy conservation properties (Remaki; 2000):

$$\mathbf{f}_{i/k} = \mathbf{f}_i\left(\frac{\vec{u}_i + \vec{u}_k}{2}\right) \tag{26}$$

Assuming constant physical properties per element and plugging the expression of the centered flux, equation 26, in equation 24 give:

$$\mathcal{M}_i \int_{V_i} \varphi_{ir}\vec{u}_i dV = -\int_{V_i} \sum_{\theta\in\{x,y,z\}} \partial_\theta\varphi_{ir}\left(\mathcal{N}_\theta\vec{u}_i\right)dV + \frac{1}{2}\sum_{k\in N_i}\int_{S_{ik}} \varphi_{ir}\mathcal{P}_{ik}\left(\vec{u}_i + \vec{u}_k\right)dS + \int_{V_i}\varphi_{ir}\vec{s}_i dV, \tag{27}$$

where $k \in N_i$ represents the elements k adjacent to the element i, S_{ik} is the face between elements i and k; and $\mathcal{P}$ is defined as follow:

$$\mathcal{P}_{ik} = \sum_{\theta\in\{x,y,z\}} n_{ik\theta}\mathcal{N}_\theta, \tag{28}$$

where $n_{ik\theta}$ is the component along the θ axis of the unit vector $\vec{n}_{ik}$ of the face S_{ik}.
Equations 27 shows that the computation of the wavefield in one element requires only information from the directly neighboring elements. This highlights clearly the local nature of the DG scheme. If we replace the expression of $\vec{u}_i$ and $\vec{u}_k$ by their decomposition on the polynomial basis, equation 19, we get:

$$\left(\mathcal{M}_i \otimes \mathcal{K}_i\right)\vec{\vec{u}}_i = -\sum_{\theta\in\{x,y,z\}}\left(\mathcal{N}_\theta \otimes \mathcal{E}_{i\theta}\right)\vec{\vec{u}}_i + \frac{1}{2}\sum_{k\in N_i}\left[\left(\mathcal{Q}_{ik}\otimes\mathcal{F}_{ik}\right)\vec{\vec{u}}_i + \left(\mathcal{Q}_{ik}\otimes\mathcal{G}_{ik}\right)\vec{\vec{u}}_k\right] + \left(\mathcal{I}\otimes\mathcal{K}_i\right)\vec{\vec{s}}_i \tag{29}$$

where the coefficients rj of the mass matrix $\mathcal{K}_i$, of the stiffness matrix $\mathcal{E}_i$ and of the flux matrices $\mathcal{F}_i$ and $\mathcal{G}_i$ are respectively given by:

$$\begin{aligned}
&\left(\mathcal{K}_i\right)_{rj} = \int_{V_i}\varphi_{ir}\varphi_{ij}dV, \quad j,r\in\left[1,d_i\right]\\
&\left(\mathcal{E}_{i\theta}\right)_{rj} = \int_{V_i}\left(\partial_\theta\varphi_{ir}\right)\varphi_{ij}dV, \quad j,r\in\left[1,d_i\right]\ \theta\in\{x,y,z\}\\
&\left(\mathcal{F}_{ik}\right)_{rj} = \int_{S_{ik}}\varphi_{ir}\varphi_{ij}dS, \quad j,r\in\left[1,d_i\right]\\
&\left(\mathcal{G}_{ik}\right)_{rj} = \int_{S_{ik}}\varphi_{ir}\varphi_{kj}dS, \quad r\in\left[1,d_i\right], j\in\left[1,d_k\right]
\end{aligned} \tag{30}$$

In equation 29, $\vec{\vec{u}}_i$ and $\vec{\vec{s}}_i$ gather all nodal values for each component of the wavefield and source. $\mathcal{I}$ is the identity matrix and $\otimes$ is the tensor product of two matrices **A** and **B**:

$$\mathbf{A}\otimes\mathbf{B} = \begin{bmatrix} a_{11}\mathbf{B} & \dots & a_{1m}\mathbf{B} \\ . & . & . \\ . & . & . \\ . & . & . \\ a_{n1}\mathbf{B} & \dots & a_{nm}\mathbf{B} \end{bmatrix} \tag{31}$$

where ($n \times m$) denotes the dimensions of the matrix $\mathbf{A}$. The four matrices $\mathcal{K}_i$, $\mathcal{E}_i$, $\mathcal{F}_{ik}$ and $\mathcal{G}_{ik}$ are computed by exact numerical integration.
It is worth noting that, in equation 30, arbitrary polynomial order of the shape functions can be used in elements i and k indicating that the approximation orders are totally decoupled from one element to another. Therefore, the DG allows for varying approximation orders in the numerical scheme, leading to the p-adaptivity.
Equation 30 can be recast in matrix form as:

$$\mathbf{A}\,\mathbf{u} = \mathbf{s} \tag{32}$$

In contrast to the parsimonious FD formulation, we do not eliminate the auxiliary velocity wavefields from the system because the elimination procedure is a cumbersome task in the DG formulation.

4.2 Which interpolation orders?

For the shape and test functions, we used low-order Lagrangian polynomials of orders 0, 1 and 2, referred to as P_k, $k \in 0, 1, 2$ in the following (Brossier; 2009; Etienne et al.; 2009). Let's remind that our motivation behind seismic modelling is to perform seismic imaging of the subsurface by full waveform inversion, the spatial resolution of which is half the propagated wavelength and that the physical properties of the medium are piecewise constant per element in our implementation of the DG method. The spatial resolution of the FWI and the piecewise constant representation of the medium direct us towards low-interpolation orders to achieve the best compromise between computational efficiency, solution accuracy and suitable discretization of the computational domain. The P_0 interpolation (or finite volume scheme) was shown to provide sufficiently-accurate solution on 2D equilateral triangular mesh when 10 cells per minimum propagated wavelength are used (Brossier et al.; 2008), while 10 cells and 3 cells per propagated wavelengths provide sufficiently-accurate solutions on unstructured triangular meshes with the P_1 and the P_2 interpolation orders, respectively (Brossier; 2009). Of note, the P_0 scheme is not convergent on unstructured meshes when centered fluxes are used (Brossier et al.; 2008). This prevents the use of the P_0 scheme in 3D medium where uniform tetrahedral meshes do not exist (Etienne et al.; 2008). A second remark is that the finite volume scheme on square cell is equivalent to second-order accurate FD stencil (Brossier et al.; 2008) which is consistent with a discretization criterion of 10 grid points per wavelength (Virieux; 1986). Use of interpolation orders greater than 2 would allow us to use coarser meshes for the same accuracy but these coarser meshes would lead to an undersampling of the subsurface model during imaging. On the other hand, use of high interpolation orders on mesh built using a criterion of 4 cells par wavelength would provide an unnecessary accuracy level for seismic imaging at the expense of the computational cost resulting from the dramatic increase of the number of unknowns in the equation 32.
The computational cost of the LU decomposition depends on the numerical bandwidth of the matrix, the dimension of the matrix (i.e., the number of rows/columns) and the number of non-zero coefficients per row (n_z). The dimension of the matrix depends in turn of the number of cell (n_{cell}), of the number of nodes per cell (n_d) and the number of wavefield components (n_{wave}) (3 in 2D and 4 in 3D). The number of nodes in a 2D triangular and 3D tetrahedral element is given by Hesthaven and Warburton (2008):

$$2D\ mesh : n_d = \frac{(k+1)(k+2)}{2},\quad 3D\ mesh : n_d = \frac{(k+1)(k+2)(k+3)}{6}, \tag{33}$$

where k denotes the interpolation order (Figure 10).

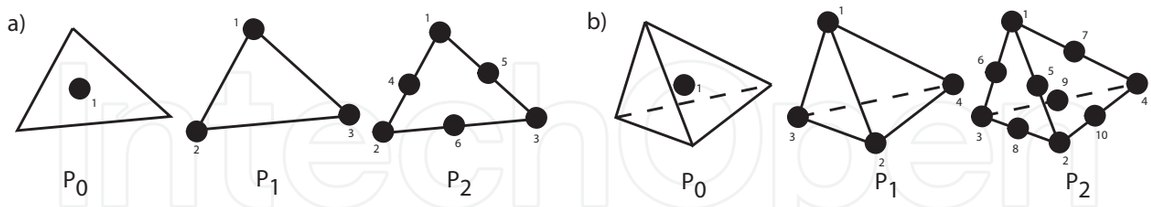

Fig. 10. Number of P_0, P_1, P_2 nodes in a triangular (a) and tetrahedral (b) element.

The numerical bandwidth is not significantly impacted by the interpolation order. The dimension of the matrix and the number of non zero elements per row of the impedance matrix are respectively given by $n_{wave} \times n_d \times n_{cell}$ and $(1+n_{neigh}) \times n_d \times n_{der} + 1$, where n_{neigh} is the number of neighbor cells (3 in 2D and 4 in 3D) and n_{der} is the number of wavefield components involved in the r.h.s of the velocity-pressure wave equation, equation 20. Table 4 outlines the number of non zero coefficients per row for the mixed-grid FD and DG methods. Increasing the interpolation order will lead to an increase of the number of non zero coefficients per row, a decrease of the number of cells in the mesh and an increase of the number of nodes in each element. The combined impact of the 3 parameters n_z, n_{cell}, n_d on the computational cost of the DG method makes difficult the definition of the optimal discretization of the frequency-domain DG method. The medium properties should rather drive us towards the choice of a suitable discretization. To illustrate this issue, we perform a numerical experiment with two end-member models composed of an infinite homogeneous and a two-layer model with a sharp velocity contrast at the base of a thin low-velocity layer. Both models have the same dimension (4 km x 4 km). The top layer of the two-layer model has a thickness of 400 m and a wave speed of 300 m/s, while the bottom layer has a wave speed of 1.5 km/s. During DG modelling, the models were successively discretized with 10 cells per minimum wavelength on an equilateral mesh for the P_0 interpolation, 10 cells per local wavelength on unstructured triangular mesh for the P_1 interpolation and 3 cells per local wavelength on unstructured triangular mesh for the P_2 interpolation. A fourth simulation was performed where P_1 interpolation is applied in the top layer while P_0 interpolation is used in the bottom layer. Table 5 outlines the time and memory requirement of the LU factorization and multi-r.h.s solve for the FD and DG methods. Among the different DG schemes, the P_2 scheme is the most efficient one in terms of computational time and memory for the two-layer model. This highlights the benefit provided by the decreasing of the number of elements in the mesh resulting from the h adaptivity coupled with a coarse discretization criterion of 3 cells per local wavelength. The mixed P_0-P_1 scheme performs reasonably well in the two-layer model although it remains less efficient than the P_2 scheme. In contrast, the performances of the P_0 and P_2 schemes are of the same order in the homogeneous model. This highlights that P_2 scheme does not provide any benefit if the h adaptivity is not required. The P_1 scheme is the less efficient one in homogeneous media because it relies on the same discretization criterion than the P_0 scheme but involves an increasing number of nodes per element. As expected, the FD method is the most efficient one in the homogeneous model thanks to the parsimonious formulation which

	FD^{2D}	$DG^{2D}_{P_0}$	$DG^{2D}_{P_1}$	$DG^{2D}_{P_2}$	FD^{3D}	$DG^{3D}_{P_0}$	$DG^{3D}_{P_1}$	$DG^{3D}_{P_2}$
n_d	1	1	3	6	1	1	4	10
n_z	9	5-9	13-25	24-48	27	6-16	21-61	51-151

Table 4. Number of nodes per element (n_d) and number of non-zero coefficients per row of the impedance matrix (n_z) for the FD and DG methods. Left: 2D case; Right: 3D case. n_z depends on the number of wavefield components involved in the r.h.s of the first-order wave equation, n_{der}, unlike the parsimonious FD method applied to the second-order wave equation.

Test	Resource	P_0	P_1	P_0-P_1	P_2	FD
Homog.	Cell/point numbers	113 097	136 724	116 363	12 222	9 604
	Degrees of freedom	339 291	1 230 516	417 477	219 996	9 604
	T_{LU} (s)	0.7	8.5	0.8	1.5	0.16
	Mem_{LU} (Gb)	1.34	5.84	1.62	1.49	0.1
	T_s (s)	11.6	40.9	13.6	7.2	0.5
Two-lay.	Cell/point numbers	2 804 850	291 577	247 303	32 664	232 324
	Degrees of freedom	8 414 550	2 624 193	1 416 243	587 952	232 324
	T_{LU} (s)	57.5	15.0	6.4	3.4	1.3
	Mem_{LU}(Gb)	31.68	11.44	5.58	3.02	1.18
	T_s (s)	274.3	83.3	46.8	18.9	2.7

Table 5. Computational ressources required for the forward problem solved with DGs P_0, P_1, P_0-P_1 and P_2 and optimized FD method in two simples cases, on 16 processors.
Nomenclature: *Homog*: homogeneous model. *Two − lay*: two-layer model. T_{LU}: time for LU factorization. Mem_{LU}: memory required by LU factorization. T_s: time for 116 r.h.s solve.

involves only the pressure wavefield and the optimized discretization criterion of 4 grid points per wavelength. The time and memory costs of the FD and P_2-DG methods are of the same order in the two-layer model. However, the P_2-DG method will be the method of choice as soon as sharp boundaries of arbitrary geometries will be present in the model due to the geometrical flexibility provided by the unstructured triangular mesh.

4.3 Boundary conditions and source implementation

Absorbing boundary conditions are implemented with unsplitted PML in the frequency-domain DG method (Brossier; 2009) following the same approach than for the FD method (see section *PML absorbing boundary conditions*). Free surface boundary condition is implemented with the method of image. A ghost cell is considered above the free surface with the same velocity and the opposite pressure components to those below the free surface. This allows us to fulfill the zero pressure condition at the free surface while keeping the correct numerical estimation of the particle velocity at the free surface. Using these particle velocities and pressures in the ghost cell, the pressure flux across the free surface interface vanishes, while the velocity flux is twice the value that would have been obtained by neglecting the flux contribution above the free surface (see equation 26). As in the FD method, this boundary condition has been implemented by modifying the impedance matrix accordingly without introducing explicitely the ghost element in the mesh. The rigid boundary condition is implemented following the same principle except that the same pressure and the opposite velocity are considered in the ghost cell. Concerning the source

excitation, the point source at arbitrary positions in the mesh is implemented by means of the Lagrange interpolation polynomials for $k \geq 1$. This means that the source excitation is performed at the nodes of the cell containing the source with appropriate weights corresponding to the projection of the physical position of the source on the polynomial basis. When the source is located in the close vicinity of a node of a triangular cell, all the weights are almost zero except that located near the source. In the case of the P_2 interpolation, a source close to the vertex of the triangular cell is problematic because the integral of the P_2 basis function over the volume of the cell is zero for nodes located at the vertex of the triangle. In this case, no source excitation will be performed (see equation 29). To overcome this problem specific to the P_2 interpolation, one can use locally a P_1 interpolation in the element containing the source at the expense of the accuracy or distribute the source excitation over several elements or express the solution in the form of local polynomials (i.e., the so-called modal form) rather than through nodes and interpolating Lagrange polynomials (i.e., the so-called nodal form). Another issue is the implementation of the source in P_0 equilateral mesh. If the source is excited only within the element containing the source, a checker-board pattern is superimposed on the wavefield solution. This pattern results from the fact that one cell out of two is excited in the DG formulation because the DG stencil does not embed a staggered-grid structure (the unexcited grid is not stored in staggered-grid FD methods; see Hustedt et al. (2004) for an illustration). To overcome this problem, the source can be distributed over several elements of the mesh or P_1 interpolation can be used in the area containing the sources and the receivers, while keeping P_0 interpolation in the other parts of the model (Brossier et al.; 2008). Of note, use of unstructured meshes together with the source excitation at the different nodes of the element contribute to mitigate the checker-board pattern in the in P_1 and P_2 schemes. The same procedure as for the source is used to extract the wavefield solution at arbitrary receiver positions.

4.4 Numerical examples

We present below two applications involving highly-contrasted media where the DG method should outperform the FD method thanks to the geometric flexibility provided by unstructured triangular or tetrahedral meshes to implement boundary conditions along interfaces of arbitrary shape.

4.4.1 Acoustic wave modelling in presence of cavities

We design a model that mimics a perfect 2D oceanic waveguide of dimension 20 000 m x 2 000 m. Applications of modelling ocean waveguide are for instance acoustic imaging of the oceanic currents, continuous monitoring of fish populations and localization of scattering sources. A free surface and a rigid surface explicit boundary conditions are implemented on the top and on the bottom of the water column to mimic the sea surface and the sea floor, respectively. A pressure source, located at position (x = 1000m; z = 1000m), propagates the direct wave in the homogeneous water layer as well as waves which are multi-reflected from the top and the bottom boundaries. Result of the simulation with the DG-P_2 scheme at 10 Hz is shown in Figure 11a. In a second simulation, we added a circular cavity of diameter 400 m in the center of the waveguide. A free surface boundary condition is implemented along the contour of the cavity. The unstructured triangular meshing around the cavity allows for an accurate discretization of the circular cavity (Figure 12).

Simulation in the waveguide with the cavity is shown in Figure 11b. Comparison with the simulation performed in the homogeneous waveguide (Figure 11a) highlights the strong interaction between the multi-reflected wavefield with the scattering source and the intrinsic non linearity of oceanic imaging resulting from complex wavepaths in the water column.

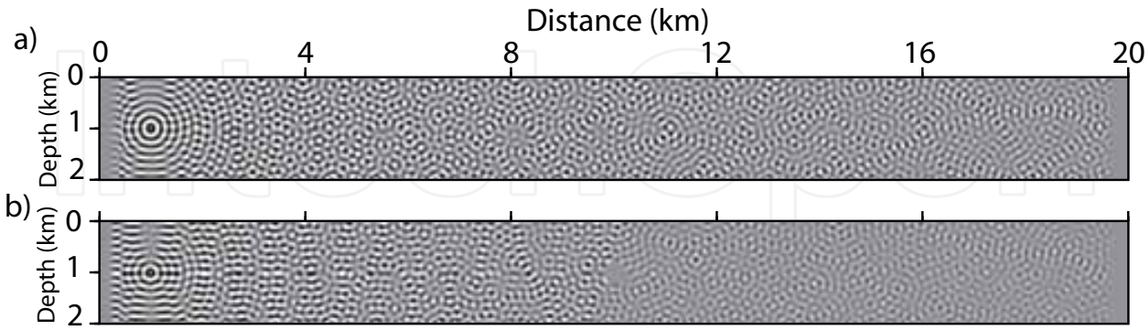

Fig. 11. Pressure wavefield in the oceanic waveguide without (a) and with (b) a circular cavity in the water column. Note that two 500-m layers of PML absorbing conditions are implemented at the two ends of the model.

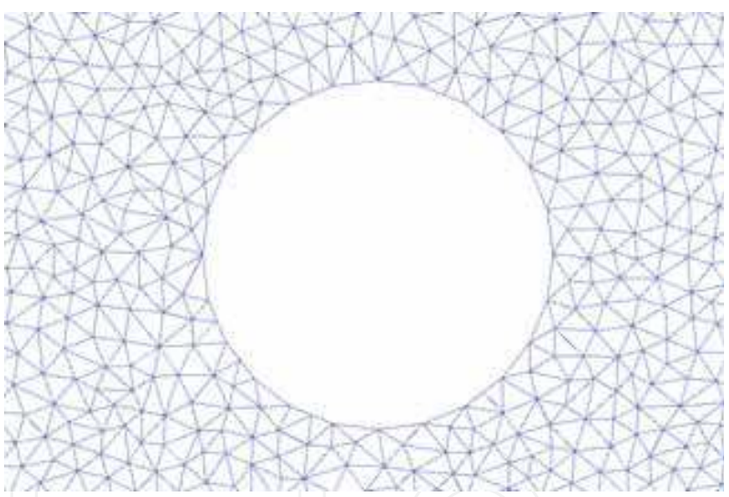

Fig. 12. Wave guide - Cavity model mesh: zoom on the cavity position.

4.4.2 Acoustic wave modelling in galleries

A second potential application of the DG method is the modelling of the air/solid contact in the framework of blast reduction in acoustic problems. The selected target illustrates the impact of the gallery design on blast reduction with application to military safety. The gallery geometry is delineated by the solid black lines in Figure 14. Due to the high wave speed contrast between the air and the solid, an adaptive mesh with a mesh refinement in the air layer was designed to minimize the number of degrees of freedom in the DG simulation (Figure 13). Figure 14(a-c) shows the horizontal velocity wavefield at the frequencies 50, 100 and 200 Hz resulting from an explosive source located near the entrance of the gallery. The wavefield in the main gallery is clearly attenuated thanks to the anti-blast first gallery and the multiple angles which hinders energy propagation.

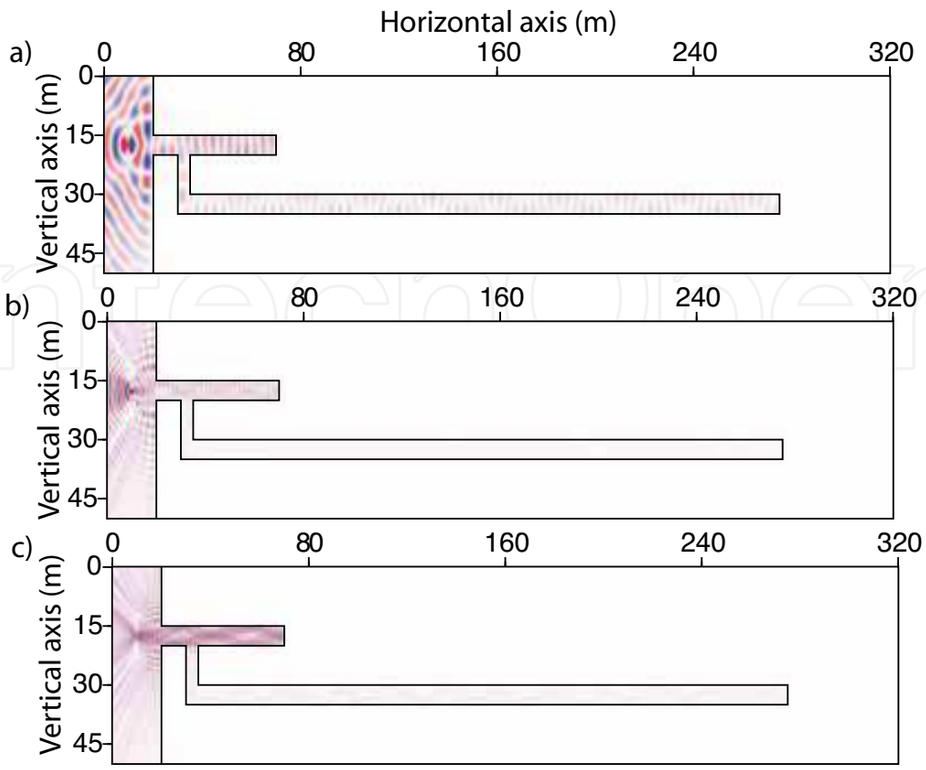

Fig. 13. (a) Gallery model geometry. Real part of the horizontal velocity wavefield at frequencies (b) 50 Hz, (c) 100 Hz and (d) 200 Hz.

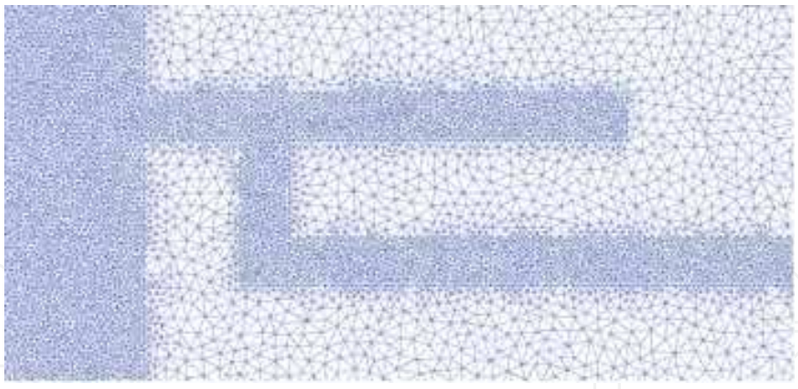

Fig. 14. Zoom on the gallery model mesh. Note the size of cells adapted to local wavespeed.

5. Conclusion and perspectives

We have reviewed two end-member numerical methods to perform visco-acoustic wave modelling in the frequency domain with sparse direct solvers. Two benefits of the frequency domain compared to the time domain are the straightforward and inexpensive implementation of attenuation effects by means of complex-valued wave speeds and the computational efficiency of multi-source modelling when a sparse direct solver is used to solve the linear system resulting from the discretization of the wave equation in the

frequency domain. The first discretization method relies on a parsimonious staggered-grid FD method based on a compact and accurate stencil allowing for both the minimization of the numerical bandwidth of the impedance matrix and the number of unknowns in the FD grid. The discretization criterion which can be used with this method is 4 grid points per minimum wavelength. We have shown the efficiency of the method for tackling 3D problems involving few millions of unknowns and few thousands of right-hand sides on computational platform composed of a limited number of processors with a large amount of shared memory. Since the FD lacks geometrical flexibility to discretize objects of complex geometries, we have developed a 2D discontinuous finite element method on unstructured triangular mesh. The DG method is fully local in the sense that each element is uncoupled from the next, thanks to the duplication of variables at nodes shared by two neighboring elements. This uncoupling allows for a flexible implementation of the so-called $h - p$ adaptivity, where the size of the element can be adapted to the local features of the model and the order of the interpolating polynomials can be adapted within each element. The price to be paid for the geometrical flexibility of the discretization is the increase of the number of unknowns compared to continuous finite element methods. We have illustrated the fields of application where the frequency-domain DG method should perform well. A first perspective of this work concerns the investigation of other linear algebra techniques to solve the linear system and overcome the limits of sparse direct solver in terms of memory requirement and limited scalability. Use of domain decomposition methods based on hybrid direct-iterative solvers should allow us to tackle 3D problems of higher dimensions. A second perspective is the improvement of the frequency-domain DG method to make possible the extension to 3D. One possible improvement is the use of heterogeneous medium properties in each element of the mesh to allow for higher-order interpolation orders. Another field of investigation concerns the numerical flux, which is a central ingredient of the DG method. Although we used centered fluxes for their energy conservation properties, other fluxes such as upwind fluxes should be investigated for improved accuracy of the scheme.

6. Acknowledgments

This study was partly funded by the SEISCOPE consortium (http://seiscope.oca.eu), sponsored by BP, CGG-Veritas, ENI, Exxon-Mobil, Shell and Total. The linear systems were solved with the MUMPS direct solver (http://graal.enslyon. fr/MUMPS). The mesh generation in DG modelling was performed with Triangle (http://www.cs.cmu.edu/ quake/triangle.html). Fill-reducing ordering was performed with METIS (http://glaros.dtc.umn.edu/gkhome/views/metis). Access to the high-performance computing facilities of SIGAMM (http://crimson.oca.eu), CINES (http://www.cines.fr) and CIMENT (OSUG) computer centers provided the necessary computer ressources. We would like to thank also Pr. G. Nolet (Geoazur) for access to the Thera cluster.

7. References

Amestoy, P. R., Guermouche, A., L'Excellent, J. Y. and Pralet, S. (2006). Hybrid scheduling for the parallel solution of linear systems, *Parallel Computing* 32: 136–156.

Aminzadeh, F., Brac, J. and Kunz, T. (1997). *3-D Salt and Overthrust models*, SEG/EAGE 3-D Modelling Series No.1.

Ben-Hadj-Ali, H., Operto, S. and Virieux, J. (2008). Velocity model building by 3D frequency-domain, full-waveform inversion of wide-aperture seismic data, *Geophysics* 73(5): VE101–VE117.

BenJemaa, M., Glinsky-Olivier, N., Cruz-Atienza, V. M. and Virieux, J. (2009). 3D Dynamic rupture simulations by a finite volume method, *Geophys. J. Int.* 178: 541–560.

BenJemaa, M., Glinsky-Olivier, N., Cruz-Atienza, V. M., Virieux, J. and Piperno, S. (2007). Dynamic non-planar crack rupture by a finite volume method, *Geophys. J. Int.* 171: 271– 285.

Berenger, J.-P. (1994). A perfectly matched layer for absorption of electromagnetic waves, *Journal of Computational Physics* 114: 185–200.

Boore, D. M. (1972). Finite-difference methods for seismic wave propagation in heterogeneous materials, *in* B. B. A. Ed. (ed.), *Methods in computational physics*, Vol. 11, Academic Press, Inc.

Brossier, R. (2009). *Imagerie sismique à deux dimensions des milieux visco-élastiques par inversion des formes d'onde: développements méthodologiques et applications.*, PhD thesis, Université de Nice-Sophia-Antipolis.

Brossier, R., Virieux, J. and Operto, S. (2008). Parsimonious finite-volume frequency-domain method for 2-D P-SV-wave modelling, *Geophys. J. Int.* 175(2): 541–559.

Chaljub, E., Komatitsch, D., Vilotte, J.-P., Capdeville, Y., Valette, B. and Festa, G. (2007). Spectral element analysis in seismology, *in* R.-S. Wu and V. Maupin (eds), *Advances in Wave Propagation in Heterogeneous Media*, Vol. 48 of *Advances in Geophysics*, Elsevier - Academic Press, pp. 365–419.

Chew, W. C. and Weedon, W. H. (1994). A 3-D perfectly matched medium from modified Maxwell's equations with stretched coordinates, *Microwave and Optical Technology Letters* 7: 599–604.

Collino, F. and Monk, P. (1998). Optimizing the perfectly matched layer, *Computer methods in Applied Mechanics and Engineering* 164: 157–171.

Collino, F. and Tsogka, C. (2001). Application of the perfectly matched absorbing layer model to the linear elastodynamic problem in anisotropic heterogeneous media, *Geophysics* 66: 294–307.

Dablain, M. A. (1986). The application of high-order differencing to the scalar wave equation, *Geophysics* 51: 54–66.

de la Puente, J., Ampuero, J.-P. and Käser, M. (2009). Dynamic Rupture Modelling on Unstructured Meshes Using a Discontinuous Galerkin Method, *J. Geophys. Res.* 114: B10302.

Demmel, J.W. (1997). *Applied numerical linear algebra*, SIAM, Philadelphia.

Dolean, V., Fol, H., Lanteri, S. and Perrussel, R. (2008). Solution of the time-harmonic Maxwell equations using discontinuous Galerkin methods, *J. Comput. Appl. Math.* 218(2): 435–445.

Dolean, V., Lanteri, S. and Perrusel, R. (2007). A domain decomposition method for solving the three-dimensional time-harmonic Maxwell equations discretized by discontinuous Galerkin methods, *J. Comput. Phys.* 227(3): 2044–2072.

Drossaert, F. H. and Giannopoulos, A. (2007). A nonsplit complex frequency-shifted PML based on recursive integration for FDTD modelling of elastic waves, *Geophysics* 72(2): T9–T17.

Duff, I. S., Erisman, A. M. and Reid, J. K. (1986). *Direct methods for sparse matrices*, Clarendon Press, Oxford, U. K.

Duff, I. S. and Reid, J. K. (1983). The multifrontal solution of indefinite sparse symmetric linear systems, *ACM Transactions on Mathematical Software* 9: 302–325.

Dumbser,M. and K¨aser,M. (2006). An Arbitrary High Order Discontinuous Galerkin Method for ElasticWaves on Unstructured Meshes II: The Three-Dimensional Isotropic Case, *Geophysical Journal International* 167(1): 319–336.

Erlangga, Y. A. and Nabben, R. (2008). Multilevel projection-based nested krylov iteration for boundary value problems, *SIAM - J. Scientific Computing* 30(3): 1572–1595.

Erlangga, Y. A., Vuik, C. and Oosterlee, C. (2006). A novel multigrid based preconditioner for heterogeneous Helmholtz problems, *SIAM - Journal of Scientific Computing* 27: 1471–1492.

Etienne, V., Brossier, R., Operto, S. and Virieux, J. (2008). A 3D Parsimonious Finite-Volume Frequency-Domain Method for ElasticWave Modelling, *Expanded Abstracts*, EAGE.

Etienne, V., Virieux, J. and Operto, S. (2009). A massively parallel time domain discontinuous Galerkin method for 3D elastic wave modelling, *SEG Technical Program Expanded Abstracts, Houston* 28(1): 2657–2661.

Faccioli, E. F., Paolucci, R. and Quarteroni, A. (1997). 2D and 3D elastic wave propagation by a pseudo-spectral domain decomposition method, *J. Seismol.* 1: 237–251.

Futterman,W. (1962). Dispersive body waves, *Journal of Geophysics Research* 67: 5279 5291.

Guermouche, A., L'Excellent, J. Y. and Utard, G. (2003). Impact of reordering on the memory of a multifrontal solver, *Parallel computing* 29: 1191–1218.

Haidar, A. (2008). *On the parallel scalability of hybrid linear solvers for large 3D problems*, PhD thesis, Institut National Polytechnique de Toulouse - CERFACS.

Hesthaven, J. S. and Warburton, T. (2008). *Nodal Discontinuous Galerkin Method. Algorithms, Analysis, and Application,* Springer.

Hicks, G. J. (2002). Arbitrary source and receiver positioning in finite-difference schemes using kaiser windowed sinc functions, *Geophysics* 67: 156–166.

Holberg, O. (1987). Computational aspects of the choice of operators and sampling interval for numerical differentiation in large-scale simulation of wave phenomena, *Geophys. Prospecting* 35: 629–655.

Hustedt, B., Operto, S. and Virieux, J. (2004). Mixed-grid and staggered-grid finite difference methods for frequency domain acoustic wave modelling, *Geophys. J. Int.* 157: 1269–1296.

Jensen, F. B., Kuperman,W. A., Porter, M. B. and Schmidt, H. (eds) (1994). *Computational ocean acoustics.*, AIP series in modern Acoustics and signal processing.

Jo, C. H., Shin, C. and Suh, J. H. (1996). An optimal 9-point, finite-difference, frequency-space 2D scalar extrapolator, *Geophysics* 61: 529–537.

Karypis, G. and Kumar, V. (1999). A fast and high quality multilevel scheme for partitioning irregular graphs, *SIAM Journal on Scientific Computing* 20(1): 359 – 392.

Kolsky, H. (1956). The propagation of stress pulses in viscoelastic solids, *Philosophical Magazine*1: 693–710.

Komatitsch, D. and Martin, R. (2007). An unsplit convolutional perfectly matched layer improved at grazing incidence for the seismic wave equation, *Geophysics* 72(5): SM155– SM167.

Komatitsch, D. and Vilotte, J. P. (1998). The spectral element method: an efficient tool to simulate the seismic response of 2D and 3D geological structures, *Bull. Seismol. Soc. Am.* 88: 368–392.

Kurzak, J. and Dongarra, J. (2006). Implementation of the mixed-precision high performance LINPACK benchmark on the CELL processor, *Technical report ut-cs-06-580, University of Tennessee. http://icl.cs.utk.edu/iter-ref/* .

Kuzuoglu, M. and Mittra, R. (1996). Frequency dependence of the constitutive parameters of causal perfectly matched anisotropic absorbers, *IEEE Microwave and Guided Wave Letters* 6: 447–449.

Langou, J., Luszczek, P., Kurzak, J., Buttari, A., and Dongarra, J. (2006). LAPACK working note 175: exploiting the performance of 32 bit floating point arithmetic in obtaining 64 bit accuracy, *Technical report, University of Tennessee. http://icl.cs.utk.edu/iter-ref/* .

LeVeque, R. J. (2002). *Finite Volume Methods for Hyperbolic Problems*, Cambridge Texts in Applied Mathematics.

Liu, J. W. H. (1992). The multifrontal method for sparse matrix solution: theory and practice, *SIAM review* 34(1): 82–109.

Lombard, B. and Piraux, J. (2004). Numerical treatment of two-dimensional interfaces for acoustic and elastic waves, *J. Compu. Physics* 195: 90–116.

Lombard, B., Piraux, J., Gelis, C. and Virieux, J. (2008). Free and smooth boundaries in 2-D finite-difference schemes for transient elastic waves, *Geophys. J. Int.* 172: 252–261.

Luo, Y. and Schuster, G. T. (1990). Parsimonious staggered grid finite-differencing of the wave equation, *Geophysical Research Letters* 17(2): 155–158.

Marfurt, K. (1984). Accuracy of finite-difference and finite-elements modelling of the scalar and elastic wave equation, *Geophysics* 49: 533–549.

Mattsson, K., Ham, F. and Iaccarino, G. (2009). Stable boundary treatment for the wave equation on second-order form, *J. Sci. Comput.* 41(3): 366–383.

Moczo, P., Kristek, J., Vavrycuk, V., Archuleta, R. and Halada, L. (2002). 3D heterogeneous staggered-grid finite-difference modelling of seismic motion with volume harmonic and arithmetic averaging of elastic moduli and densities, *Bull. Seismol. Soc. Am.* 92: 3042–3066.

MUMPS-team (2009). *MUMPS - MUltifrontal Massively Parallel Solver users' guide - version 4.9.2 (November 2009)*, ENSEEIHT-ENS Lyon, http://www.enseeiht.fr/apo/MUMPS/ or http://graal.ens-lyon.fr/MUMPS.

Operto, S., Virieux, J., Amestoy, P., L' Éxcellent, J.-Y., Giraud, L. and Ben-Hadj-Ali, H. (2007). 3D finite-difference frequency-domain modelling of visco-acoustic wave propagation using a massively parallel direct solver: A feasibility study, *Geophysics* 72(5): SM195– SM211.

Operto, S., Virieux, J., Ribodetti, A. and Anderson, J. E. (2009). Finite-difference frequency-domain modelling of visco-acoustic wave propagation in two-dimensional TTI media, *Geophysics* 74 (5): T75–T95.

Pitarka, A. (1999). 3D elastic finite-difference modelling of seismic motion using staggered grids with nonuniform spacing, *Bull. Seism. Soc. Am.* 89(1): 54–68.

Plessix, R. E. (2007). A Helmholtz iterative solver for 3D seismic-imaging problems, *Geophysics* 72(5): SM185–SM194.

Priolo, E., Carcione, J. M. and Seriani, G. (1994). Numerical simulation of interface waves by high-order spectral modelling techniques, *J. acoust. Soc. Am.* 95: 681–693.

Remaki, M. (2000). A new finite volume scheme for solving Maxwell's system, *COMPEL* 19(3): 913–931.

Riyanti, C. D., Erlangga, Y. A., Plessix, R. E., Mulder, W. A., Vuik, C. and Oosterlee, C. (2006). A new iterative solver for the time-harmonic wave equation, *Geophysics* 71(E): 57–63.

Riyanti, C. D., Kononov, A., Erlangga, Y. A., Vuik, C., Oosterlee, C., Plessix, R. E. and Mulder, W. A. (2007). A parallel multigrid-based preconditioner for the 3D heterogeneous high-frequency Helmholtz equation, *Journal of Computational physics* 224: 431–448.

Roden, J. A. and Gedney, S. D. (2000). Convolution PML (CPML): An efficient FDTD implementation of the CFS-PML for arbitrary media, *Microwave and Optical Technology Letters* 27(5): 334–339.

Saad, Y. (2003). *Iterative methods for sparse linear systems,* SIAM, Philadelphia.

Saenger, E. H., Gold, N. and Shapiro, S. A. (2000). Modelling the propagation of elastic waves using a modified finite-difference grid, *Wave motion* 31: 77–92.

Sen, M. K. and Stoffa, P. L. (1995). *Global Optimization Methods in Geophysical Inversion*, Elsevier Science Publishing Co.

Seriani, G. and Priolo, E. (1994). Spectral element method for acoustic wave simulation in heterogeneous media, *Finite elements in analysis and design* 16: 337–348.

Sirgue, L., Etgen, J. T. and Albertin, U. (2008). 3D Frequency Domain Waveform Inversion using Time Domain Finite Difference Methods, *Proceedings 70th EAGE, Conference and Exhibition, Roma, Italy*, p. F022.

Smith, B. F., Bjørstad, P. E. and Gropp, W. (1996). *Domain decomposition: parallel multilevel methods for elliptic partial differential equations,* Cambridge University Press.

Sourbier, F., Haidar, A., Giraud, L., Operto, S. and Virieux, J. (2008). Frequency-domain full-waveform modelling using a hybrid direct-iterative solver based on a parallel domain decomposition method: A tool for 3D full-waveform inversion?, *SEG Technical Program Expanded Abstracts* 27(1): 2147–2151.

Stekl, I. and Pratt, R. G. (1998). Accurate viscoelastic modelling by frequency-domain finite difference using rotated operators, *Geophysics* 63: 1779–1794.

Taflove, A. and Hagness, C. (2000). *Computational electrodynamics: the finite-difference time-domaine method*, Artech House, London, United Kindom.

Takeuchi, N. and Geller, R. J. (2000). Optimally accurate second-order time-domain finite-difference scheme for computing synthetic seismograms in 2-D and 3-D media, *Phys. Earth planet. Inter.* 119: 99–131.

Virieux, J. (1986). P-SV wave propagation in heterogeneous media, velocity-stress finite difference method, *Geophysics* 51: 889–901.

Virieux, J. and Operto, S. (2009). An overview of full waveform inversion in exploration geophysics, *Geophysics* 74(6): WCC127–WCC152.

Virieux, J., Operto, S., Ben-Hadj-Ali, H., Brossier, R., Etienne, V., Sourbier, F., Giraud, L. and Haidar, A. (2009). Seismic wave modelling for seismic imaging, *The Leading Edge* 28(5): 538–544.

Yee, K. S. (1966). Numerical solution of initial boundary value problems involving Maxwell's equations in isotropic media, *IEEE Trans. Antennas and Propagation* 14: 302–307.

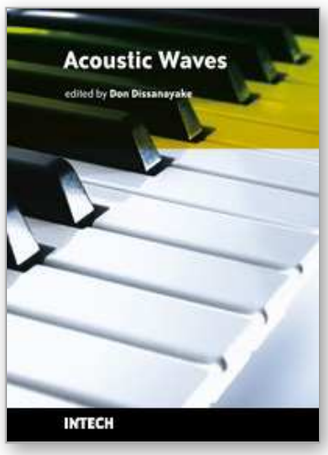

Acoustic Waves
Edited by Don Dissanayake

ISBN 978-953-307-111-4
Hard cover, 434 pages
Publisher Sciyo
Published online 28, September, 2010
Published in print edition September, 2010

SAW devices are widely used in multitude of device concepts mainly in MEMS and communication electronics. As such, SAW based micro sensors, actuators and communication electronic devices are well known applications of SAW technology. For example, SAW based passive micro sensors are capable of measuring physical properties such as temperature, pressure, variation in chemical properties, and SAW based communication devices perform a range of signal processing functions, such as delay lines, filters, resonators, pulse compressors, and convolvers. In recent decades, SAW based low-powered actuators and microfluidic devices have significantly added a new dimension to SAW technology. This book consists of 20 exciting chapters composed by researchers and engineers active in the field of SAW technology, biomedical and other related engineering disciplines. The topics range from basic SAW theory, materials and phenomena to advanced applications such as sensors actuators, and communication systems. As such, in addition to theoretical analysis and numerical modelling such as Finite Element Modelling (FEM) and Finite Difference Methods (FDM) of SAW devices, SAW based actuators and micro motors, and SAW based micro sensors are some of the exciting applications presented in this book. This collection of up-to-date information and research outcomes on SAW technology will be of great interest, not only to all those working in SAW based technology, but also to many more who stand to benefit from an insight into the rich opportunities that this technology has to offer, especially to develop advanced, low-powered biomedical implants and passive communication devices.

InTech Europe
University Campus STeP Ri
Slavka Krautzeka 83/A

InTech China
Unit 405, Office Block, Hotel Equatorial Shanghai
No.65, Yan An Road (West), Shanghai, 200040, China

51000 Rijeka, Croatia
Phone: +385 (51) 770 447
Fax: +385 (51) 686 166
www.intechopen.com

中国上海市延安西路65号上海国际贵都大饭店办公楼405单元
Phone: +86-21-62489820
Fax: +86-21-62489821

IntechOpen

IntechOpen